IEEE Access
Multidisciplinary ⋮ Rapid Review ⋮ Open Access Journal

Received August 17, 2019, accepted August 21, 2019, date of publication August 26, 2019, date of current version September 10, 2019.

Digital Object Identifier 10.1109/ACCESS.2019.2937390

Quantum Image Watermarking Algorithm Based on Haar Wavelet Transform

WEN-WEN HU[1,2], RI-GUI ZHOU[1,2], (Member, IEEE), AHMED EL-RAFEI[3], (Member, IEEE), AND SHE-XIANG JIANG[1,2]

[1]College of Information Engineering, Shanghai Maritime University, Shanghai 201306, China
[2]Research Center of Intelligent Information Processing and Quantum Intelligent Computing, Shanghai 201306, China
[3]Engineering Physics and Mathematics Department, Faculty of Engineering, Ain Shams University, Cairo 11517, Egypt

Corresponding author: Ri-Gui Zhou (rgzhou@shmtu.edu.cn)

This work was supported in part by the National Key Research and Development Plan under Grant 2018YFC1200200 and Grant 2018YFC1200205, in part by the National Natural Science Foundation of China under Grant 61463016, and in part by the Science and Technology Innovation Action Plan of Shanghai in 2017 under Grant 17510740300.

ABSTRACT In this paper, a novel frequency domain quantum watermarking scheme is proposed based on the Flexible Representation of Quantum Images, which can embed a $2^{n1} \times 2^{n1}$ binary watermark image into a $2^n \times 2^n$ grayscale carrier image. The quantum Haar wavelet transform is developed and used to decompose quantum images. The diagonal detail coefficients of the carrier image are obtained from the image decomposition. Then, according to the watermark image information, the diagonal wavelet coefficients are either unchanged or slightly modified. Since all of the used quantum operations are invertible, extraction of the watermark image is performed in a straightforward manner by reversing the watermarking embedding process. Finally, the proposed quantum image watermarking scheme is simulated on a classical computer and evaluated under different carrier and watermark images. The simulation results and performance analyses indicate the high performance of the presented watermarking scheme in terms of the similarity between the watermarked and carrier images.

INDEX TERMS Quantum computing, qubit, digital images, discrete wavelet transforms, image decomposition, wavelet coefficients, watermarking, computational complexity, circuit simulation.

I. INTRODUCTION

A. BACKGROUND

Quantum Information Processing (QIP) represents a novel computing and processing paradigm model rather than the classical model based on conventional computers. Information is stored in quantum registers and regarded as quantum bits (qubits) [1]. Thus, information can be stored, processed, and transmitted utilizing the peculiar aspects of quantum mechanics. The inherent properties in the theory of quantum mechanics, such as quantum coherence, entanglement, and superposition of quantum states make quantum computing superior to its classical counterpart for information storage and processing [2]. Therefore, quantum computation might offer a possible solution to the current challenge posed by the failure of Moore's law [3]. Quantum algorithms such as Shor's discrete logarithms and integer factoring algorithms in polynomial time [4], Deutsch's parallel computing algorithm with quantum parallelism and coherence [5], and Grover's quadratic speedup for unordered database search algorithms [6] achieve higher performance than any known classical algorithms. As a result of the rapid development of quantum computation, classical image processing is naturally extended to the quantum domain. Despite the physical limitations in realizing the fully and efficiently functional quantum computers, it is important to be able to perform different information processing tasks on a quantum computer once it is practically implemented in the near future. Quantum image processing is an emerging sub-discipline that focuses on porting conventional image processing tasks and operations to the quantum computing framework [7], [8]. It is primarily devoted to utilizing quantum computing technologies to represent, recover, and perform operations on quantum images in various formats for different purposes [8], [9].

There are two aspects of quantum image processing: quantum image representations and quantum image processing algorithms. At present, many quantum image representation models have been investigated [10]–[18]. Wherein,

The associate editor coordinating the review of this article and approving it for publication was Gerard-Andre Capolino.

the Flexible Representation of Quantum Images (FRQI) and Novel Enhanced Quantum Representation (NEQR) of digital images are the most two commonly used quantum image representation models.

Steganography and watermarking are closely related fields with a great deal of overlap and share many technical approaches [19]. Generally, the purpose of steganography is to hide the existence of a message by embedding symbolic information into public data. Watermarking has been considered for many copy prevention and copyright protection applications by inserting author related information into a signal or image. The watermark information is typically used to identify the copyright holder and ensures proper payment of royalties.

Quantum image watermarking has recently received considerable attention. Based on the developed quantum image representation models, many watermarking techniques have been proposed [20]–[26]. The scheme proposed in this paper falls into the category of quantum image watermarking methods. Thus, the existing works in the literature related to this category are discussed in the next section.

B. CONTRIBUTIONS

In digital image processing, Discrete Wavelet Transforms (DWT) has been shown to be quite effective in important applications such as image compression and signal processing [27], [28]. DWT-based image watermarking utilizes the multi-resolution characteristics of an image and resembles the operation of human vision [29], [30]. The human eye has less sensitivity to small changes in high frequency content, such as edges and texture, than to changes in low frequency features, such as the average luminance of an image. In hierarchical analysis using DWT, the edges and textures are contained in the high frequency subbands. Wavelet coefficients with large values in these subbands usually indicate edges in an image. Therefore, it would be highly efficient to hide the watermarking information into these coefficients as it will be undetected by the human eye.

In this work, the quantum Haar wavelet transforms (QHWT) is developed along with its quantum circuit implementation. Based on the introduced QHWT, a quantum image watermarking algorithm in the frequency domain is proposed for FRQI. The QHWT can be applied to decompose a quantum image modeled by FRQI. Using the multi-resolution analysis, the quantum carrier image can be decomposed into any desired level resulting in four subbands: approximate subband, horizontal subband, vertical subband, and diagonal subband. The watermarking information is chosen to be inserted into the diagonal subband. This is because the information in this subband is typically less significant than the information in the other subbands, and thus has a slight influence on the quality of the reconstructed image.

The main contributions of this work are: (1) the development and application of QHWT to decompose quantum images represented by FRQI and the design of a corresponding quantum circuit; (2) Based on the developed QHWT, two novel quantum image watermarking schemes, non-block and block watermarking algorithms, are proposed to insert watermark image information into the carrier image's diagonal wavelet coefficients of the high frequency subband. To the best of our knowledge, the presented watermarking scheme is the first correctly functional quantum watermarking scheme in the frequency domain as discussed in the next subsection. Moreover, the proposed method is shown to be highly efficient in watermarking quantum images using various measures in comparison to other methods.

The rest of this paper is organized as follows. Section II includes a survey of the state of the art in quantum image watermarking. The basic topics needed for the development of the proposed algorithm, including quantum gates, FRQI image, and the Haar wavelet transforms (HWT), are provided in Section III. In Section IV, we introduce the circuit design for QHWT and the corresponding effective circuits for multi-level decomposition of FRQI images. Quantum watermark image embedding and extracting schemes, quantum measurement operation for FRQI images, and circuit complexity analysis are discussed in detail in Section V. Simulations on classical computer and experimental results as well as performance analyses are given in Section VI. Finally, the conclusions and future works are stated in Section VII.

II. RELATED WORKS

The methods developed for quantum image watermarking can be categorized based on their domain of operation: spatial domain [20]–[23] and frequency domain [24]–[26]. The algorithms in the first category insert the watermarking information in the spatial domain. The second class utilizes transforms to convert the image into the frequency domain and perform the embedding process in this domain.

Spatial quantum image watermarking schemes were proposed based on the NEQR model, such as Arnold transforms and Least Significant Bit (LSB) based quantum image watermarking [20], LSBs-based quantum image watermarking in edge regions [21], [22], and LSBs-based quantum image watermarking using gray code transformation [23]. Note that because the NEQR model utilizes q qubits computational basis states to encode the pixel color information, Quantum Fourier transform (QFT) [3], [31] and Quantum wavelet transform (QWT) [32] cannot be applied to decompose images based on the NEQR model. On the contrary, the FRQI model encodes the pixel color information in the amplitude of a single qubit based on angle encoding via quantum unitary rotation operation. This allows the decomposition of images using QFT and QWT, which facilitates the design of quantum image processing algorithms, such as quantum image encryption schemes [33], [34]. Therefore, transform-based quantum watermarking schemes that utilized the FRQI model were investigated, such as watermarking using quantum Fourier transform [24], quantum wavelet transform [25], and Hadamard transform [26].

The aforementioned frequency domain algorithms [24]–[26] based on the FRQI model are not accurate as

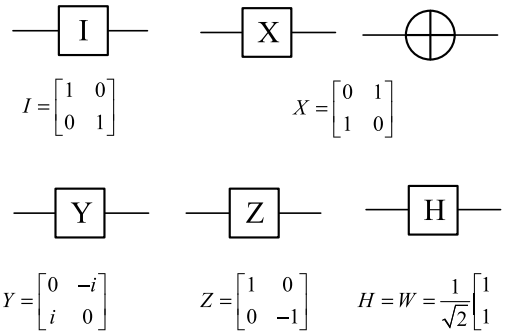

FIGURE 1. Single qubit Pauli (I, X, Y, and Z) and Hadamard (H) gates along with their corresponding matrices' representation.

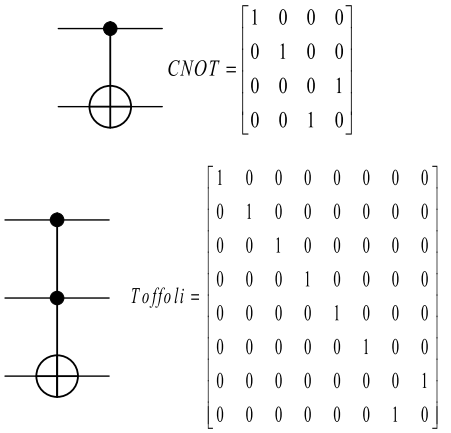

FIGURE 2. Quantum circuits and matrices of CNOT and Toffoli gates.

proven in [35]–[37]. This is because the pixel color information of the FRQI image is encoded by a single qubit's amplitude. Therefore, the methods in [24]–[26], applied to FRQI images by adding the grayscale information of quantum watermark image directly to the carrier image information, which violate the principles of quantum mechanics. Specifically, the quantum watermarking scheme [24] is infeasible because it simply adds the weighted grayscale information of the quantum watermark image to the Fourier coefficients of the carrier image. Similarly, the quantum watermarking methods in [25], [26] use a plain adder network to add the grayscale information of the quantum watermark image to the carrier image information. This is also incorrect because the inputs of two registers in a plain adder network should be encoded in binary form in the computational basis states.

III. PRELIMINARIES

A. QUANTUM GATES

Quantum computation is implemented via quantum unitary operators, which are constructed using quantum gates. Quantum operations on a single qubit or multiple qubits are described by unitary matrices. Among the most common single qubit gates are the Pauli operators (denoted as I, X, Y and Z) and Hadamard transform (denoted as H or W). The quantum circuits of the aforementioned gates and their equivalent matrices are illustrated in Fig. 1.

Note that the X gate is usually referred to as the NOT gate, commonly denoted by another notation $\oplus$. The Controlled-NOT (CNOT) and Toffoli gates are examples of important two-qubit and three qubit gates, respectively, of these multiple qubits. Figure 2 shows the CNOT and Toffoli quantum circuits and their corresponding matrices.

More complex multiple qubits gates can be decomposed into sa series of basic quantum logic gates, such as NOT, CNOT, and Toffoli gates. In [3], [38], single qubit and two-qubit gates are considered be universal in the sense that all unitary operations on arbitrary many n qubits can be performed using them as building blocks.

In addition to the above mentioned basic quantum gates, two other important single qubit unitary gates have the following matrix forms:

$$R_y(2\varphi)=\begin{bmatrix}\cos\varphi & -\sin\varphi\\ \sin\varphi & \cos\varphi\end{bmatrix},$$
$$C(2\varphi)=\begin{bmatrix}\cos\varphi & \sin\varphi\\ \sin\varphi & -\cos\varphi\end{bmatrix} \quad (1)$$

when these matrices operate on a single qubit $|\psi\rangle = \cos\xi\,|0\rangle + \sin\xi\,|1\rangle = [\cos\xi\ \sin\xi]^T$, the outcome can be expressed as:

$$\begin{aligned}R_y(2\varphi)|\psi\rangle &= \begin{bmatrix}\cos\varphi & -\sin\varphi\\ \sin\varphi & \cos\varphi\end{bmatrix}\begin{bmatrix}\cos\xi\\ \sin\xi\end{bmatrix}\\ &= \begin{bmatrix}\cos\varphi\cos\xi-\sin\varphi\sin\xi\\ \sin\varphi\cos\xi+\cos\varphi\sin\xi\end{bmatrix}\\ &= \cos(\varphi+\xi)|0\rangle+\sin(\varphi+\xi)|1\rangle\\ C(2\varphi)|\psi\rangle &= \begin{bmatrix}\cos\varphi & \sin\varphi\\ \sin\varphi & -\cos\varphi\end{bmatrix}\begin{bmatrix}\cos\xi\\ \sin\xi\end{bmatrix}\\ &= \begin{bmatrix}\cos\varphi\cos\xi+\sin\varphi\sin\xi\\ \sin\varphi\cos\xi-\cos\varphi\sin\xi\end{bmatrix}\\ &= \cos(\varphi-\xi)|0\rangle+\sin(\varphi-\xi)|1\rangle \quad (2)\end{aligned}$$

Obviously, unitary gates $R_y(2\varphi)$ and $C(2\varphi)$ are single-qubit rotation gates. When operating on single qubit $|\psi\rangle = \cos\xi\,|0\rangle + \sin\xi\,|1\rangle$, $R_y(2\varphi)$ changes the angle ξ to $\xi+\varphi$ while $C(2\varphi)$ changes ξ to $\varphi-\xi$.

The two unitary matrices $R_y(2\varphi)$ and $C(2\varphi)$ with multiple controlled qubits are illustrated in Fig. 3, in which white and black points denote the qubit in computational basis states $|0\rangle$ and $|1\rangle$, respectively. The unitary matrices $R_y(2\varphi)$ and $C(2\varphi)$ will not change the last qubit unless the qubit sequence states are the same as the control qubit sequence. In other words, when the bit sequence is $a_{n-1}a_{n-2}a_{n-3}\cdots a_2a_1 = 101\cdots01$, qubit $|a_0\rangle$ would change to $R_y(2\varphi)|a_0\rangle$ or $C(2\varphi)|a_0\rangle$, otherwise, it will apply the identity gate I on qubit $|a_0\rangle$ leaving it unchanged.

B. FLEXIBLE REPRESENTATION OF QUANTUM IMAGES

Flexible representation of quantum images (FRQI) proposed in [12] encodes the information of a $2^n \times 2^n$ digital image in

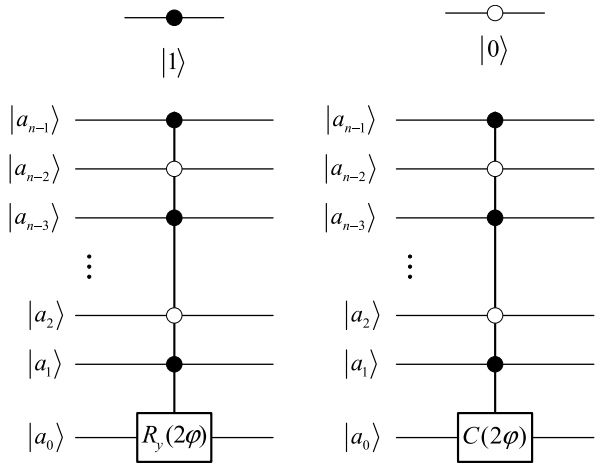

FIGURE 3. Quantum circuits for unitary operations R_y (2φ) and C (2φ) under multiple controlled qubits cases.

the following quantum state:

$$|I(\theta)\rangle = \frac{1}{2^n}\sum_{i=0}^{2^{2n}-1}|C_i\rangle|i\rangle = \frac{1}{2^n}\sum_{i=0}^{2^{2n}-1}(\cos\theta_i|0\rangle + \sin\theta_i|1\rangle)|i\rangle$$
$$\theta_i \in \left[0, \frac{\pi}{2}\right], \quad i = 0, 1, 2, \cdots, 2^{2n}-1 \tag{3}$$

where $|0\rangle$ and $|0\rangle$ are the two-dimensional quantum computational basis states, $|i\rangle, i = 1, 2, \cdots, 2^{2n}-1$ are the 2^{2n}-dimensional quantum computational basis states, and $\theta = [\theta_0, \theta_1, \cdots, \theta_{2^{2n}-2}, \theta_{2^{2n}-1}]$ is the vector of angle encoding colors.

The FRQI representation model integrates the information in an image within two variables: $|i\rangle = |Y\rangle|X\rangle$ denotes the pixel location information, where $|X\rangle = |x_{n-1}x_{n-2}\cdots x_1x_0\rangle$ and $|Y\rangle = |y_{n-1}y_{n-2}\cdots y_1y_0\rangle$ represent the coordinate information in the horizontal and vertical directions, respectively; $|C_i\rangle = \cos\theta_i|0\rangle + \sin\theta_i|1\rangle$ encodes the pixel color information in position $|i\rangle$. Therefore, it is easy to deduce that $(1+2n)$ qubits are needed to encode a $2^n \times 2^n$ digital image in a quantum register based on the FRQI model.

Applying basic quantum gate Z to the pixel color information $|C_i\rangle$ yields:

$$Z|C_i\rangle = \begin{bmatrix}1 & 0\\ 0 & -1\end{bmatrix}\begin{bmatrix}\cos\theta_i\\ \sin\theta_i\end{bmatrix} = \begin{bmatrix}\cos\theta_i\\ -\sin\theta_i\end{bmatrix}$$
$$= \cos(-\theta_i)|0\rangle + \sin(-\theta_i)|1\rangle \tag{4}$$

For binary and grayscale images, the FRQI model uses the bijective function to convert a fixed color C_i to an angle θ_i as given by (5).

$$\theta_i = \frac{\pi}{2}\times C_i, \quad \textit{binary image}, \ C_i = 0, 1$$
$$\theta_i = \frac{\pi}{2}\times\frac{C_i}{255}, \quad \textit{grayscale image}, \quad C_i = 0, 1, \cdots, 255 \tag{5}$$

Based on the FRQI representation model, a color image can be expressed via three channels of Red, Green and Blue

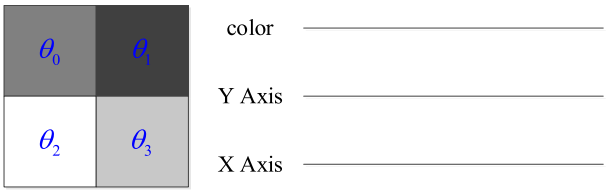

$$|I\rangle = \frac{1}{2}\Big[(\cos\theta_0|0\rangle + \sin\theta_0|1\rangle)|00\rangle + (\cos\theta_1|0\rangle + \sin\theta_1|1\rangle)|01\rangle$$
$$+ (\cos\theta_2|0\rangle + \sin\theta_2|1\rangle)|10\rangle + (\cos\theta_3|0\rangle + \sin\theta_3|1\rangle)|11\rangle\Big]$$

FIGURE 4. A 2 × 2 FRQI image, and its quantum wire diagram, and expression.

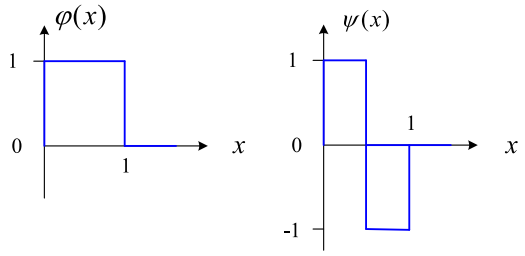

FIGURE 5. Waveform of the Haar basis function $\varphi(x)$ and Haar wavelet function $\psi(x)$.

as follows [29]:

$$|I\rangle = \frac{1}{2^n}\sum_{i=0}^{2^{2n}-1}|C_i\rangle\otimes|i\rangle, \quad |C_i\rangle = |r_i\rangle|g_i\rangle|b_i\rangle$$
$$|k_i\rangle = \cos\theta_{k_i}|0\rangle + \sin\theta_{k_i}|1\rangle, \quad k = r, g, b$$
$$\theta_i \in \left[0, \frac{\pi}{2}\right], \quad i = 0, 1, 2, \cdots, 2^{2n}-1 \tag{6}$$

An example of a 2 × 2 FRQI grayscale image is demonstrated in Fig. 4, where the corresponding quantum circuit and representative expression are shown on its right and below, respectively.

C. HAAR WAVELET TRANSFORMS AND DECOMPOSITION OF DIGITAL IMAGES

HWT is constructed from the Haar basis function $\varphi(x)$ and Haar wavelet function $\psi(x)$ [39], [40], which are defined in (7). Their corresponding waveforms are shown in Fig. 5.

$$\varphi(x) = \begin{cases}1, & x\in[0,1)\\ 0, & \text{the}-\text{other},\end{cases} \qquad \psi(x) = \begin{cases}1, & x\in[0,1/2)\\ -1, & x\in[1/2,1)\\ 0, & \text{the other}\end{cases} \tag{7}$$

Scaled and shifted versions of the functions $\varphi(x)$ and $\psi(x)$ are used to construct different vector spaces V and W. The vector spaces V^j and W^j spanned by the j-scaled versions of $\varphi(x)$ and $\psi(x)$, respectively, have the property of $V^{j+1} = V^j \oplus W^j$, where the symbol $\oplus$ stands for direct sum. This results in the following two properties: (1) Linear spaces W^j and V^j can construct a new linear space V^{j+1}; (2) Each

basis function in the vector space W^j is orthogonal to the basis function in the vector space V^j.

Based on the HWT, a signal can be decomposed into its low frequency and high frequency content captured by $\varphi(x)$ and $\psi(x)$, respectively. The HWT coefficients can be computed by iteratively calculating the mean and difference of signal values representing the approximate and detailed information, respectively. The reconstruction of the original signal from the wavelet coefficients by the inverse of the transform is straightforward.

HWT can be easily extended from the one-dimensional signal case to analysis of two-dimensional images. The standard decomposition can be performed by applying the HWT on all of the row pixels in the image, then, on the columns of the transformed image.

Suppose M is used to denote the matrix of HWT and F is the pixel matrix of a two-dimensional image. Then, the standard decomposition (D) of HWT for the two-dimensional digital image F and its inverse transform can be expressed as:

$$D = \left((FM)^T M\right)^T = M^T F M,$$
$$F = \left(M^T\right)^{-1} D M^{-1} \tag{8}$$

where $(M)^T$ is the transpose of matrix M and $(M)^{-1}$ is the inverse matrix of M.

IV. CIRCUIT FOR QUANTUM HWT AND DECOMPOSITION OF FRQI IMAGE

Data storage and processing in quantum registers are quite different than in the classical domain. Mathematically, quantum information is encoded in Hilbert vector space and can be stored in a superposition state. Quantum operations are described and realized by applying a series of unitary matrices of size $2^n \times 2^n$ for an n-qubit quantum register. In this section, we introduce efficient quantum circuits for QHWT. Then based on the developed QHWT, quantum multi-scale image decomposition for an FRQI image is proposed and detailed.

A. EFFECTIVE CIRCUIT FOR QHWT

Prior to introducing the integrated quantum circuit for QHWT, the details of two important elements of the circuit are described [32]. The first element is the Wash-Hadamard gate (W) (or Hadamard (H) gate) with the matrix form $W = H = 1/\sqrt{2}\begin{bmatrix} 1 & 1 \\ 1 & -1 \end{bmatrix}$. When the W gate operates on the pure state of a single qubit $|\psi\rangle = a|0\rangle + \beta|1\rangle$, the result is:

$$W|\psi\rangle = \frac{1}{\sqrt{2}}\begin{bmatrix} 1 & 1 \\ 1 & -1 \end{bmatrix}\begin{bmatrix} a \\ \beta \end{bmatrix} = \frac{1}{\sqrt{2}}\begin{bmatrix} a+\beta \\ a-\beta \end{bmatrix} \tag{9}$$

The second element is the permutation operator Π_{2^n}. When Π_{2^n} is applied to an n-qubit quantum registers $|a_{n-1}a_{n-2}\cdots a_1a_0\rangle$, it yields:

$$\Pi_{2^n}|a_{n-1}a_{n-2}\cdots a_1a_0\rangle = |a_0a_{n-1}a_{n-2}\cdots a_1\rangle \tag{10}$$

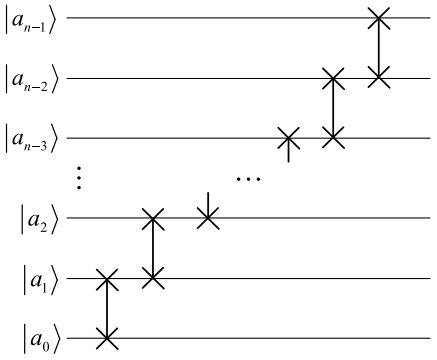

FIGURE 6. Quantum circuit for the permutation operator Π_{2^n}.

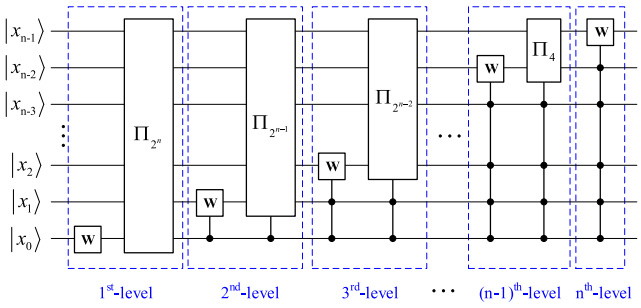

(a) Circuit for full levels QHWT

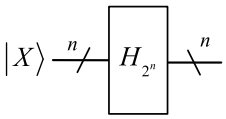

(b) The diagram of full levels QHWT

FIGURE 7. Quantum circuit for full levels QHWT and its simplified diagram.

For example, the two-qubit permutation operator Π_4 is a Swap gate. The n-qubit operator Π_{2^n} can be realized through a series application of the Π_4 gate as illustrated in Fig. 6.

According to the quantum circuit illustrated in Fig. 6, the unitary matrix for n-qubit permutation operation Π_{2^n} can be written as:

$$\Pi_{2^n} = \left(\Pi_4 \otimes I_2^{\otimes n-2}\right)\left(I_2 \otimes \Pi_4 \otimes I_2^{\otimes n-3}\right) \cdots \left(I_2^{\otimes n-3} \otimes \Pi_4 \otimes I_2\right)\left(I_2^{\otimes n-2} \otimes \Pi_4\right) \tag{11}$$

where $I_2^{\otimes n-2}$ is the tensor product of the second-order identity matrix multiplied (n-2) times.

Based on the two circuit elements above, a quantum circuit for n-qubit QHWT is implemented by decomposing the integrated circuit into a sequence of matrix multiplication operations, direct sum, and tensor product as demonstrated in Fig. 7.

Accordingly, the matrix form of the QHWT H_{2^n} that corresponds to the circuit in Fig. 7 is:

$$\begin{aligned} H_{2^n} = & \left(W \oplus I_{2^n-2}\right)\left(\Pi_4 \oplus I_{2^n-4}\right)\left(I_2 \otimes W \oplus I_{2^n-4}\right) \\ & \cdots \left(\Pi_{2^{n-i+1}} \oplus I_{2^n-2^{n-i+1}}\right)\left(I_{2^{n-i}} \otimes W \oplus I_{2^n-2^{n-i+1}}\right) \\ & \cdots \left(\Pi_{2^{n-2}} \oplus I_{2^n-2^{n-2}}\right)\left(I_{2^{n-3}} \otimes W \oplus I_{2^n-2^{n-2}}\right) \\ & \times \left(\Pi_{2^{n-1}} \oplus I_{2^n-2^{n-1}}\right)\left(I_{2^{n-2}} \otimes W \oplus I_{2^n-2^{n-1}}\right) \\ & \times \Pi_{2^n}\left(I_{2^{n-1}} \otimes W\right) \end{aligned} \tag{12}$$

B. DECOMPOSITION FOR FRQI IMAGE

For a two-dimensional digital image, there are two ways to transform an image based on HWT: standard decomposition and non-standard decomposition [40]. The standard decomposition method refers to transforming the image's pixel values in each row using a one-dimensional HWT. This is followed by transforming the columns of the row-transformed image by using a one-dimensional HWT again. In contrast, non-standard decomposition is obtained by alternating the application of the one-dimensional HWT along the horizontal and vertical directions.

The quantum image representation model FRQI utilizes the quantum computational basis states to encode all of the pixel coordinate position information and stores it into a superposition state. Thus, quantum image decomposition based on standard QHWT decomposition is simpler and more suitable for implementation as a quantum circuit than the non-standard decomposition.

Assume we have a $2^n \times 2^n$ FRQI grayscale image expressed as below:

$$\begin{aligned} |C\rangle &= \frac{1}{2^n}\sum_{Y=0}^{2^n-1}\sum_{X=0}^{2^n-1} |f(Y,X)\rangle\,|YX\rangle\,, \\ |f(Y,X)\rangle &= \cos\theta_{YX}\,|0\rangle + \sin\theta_{YX}\,|0\rangle \end{aligned} \tag{13}$$

Figure 8 shows the integrated quantum circuit for standard n-level decomposition of an FRQI image using the QHWT circuit in Fig. 7(a) that is performed in the following two steps:

Step 1 (Row Decomposition): Row decomposition is realized by applying the H_{2^n} matrix to the FRQI image's coordinate qubits $|X\rangle = |x_{n-1}x_{n-2}\cdots x_1x_0\rangle$ in the horizontal direction. If we define the matrix at this stage as H_{row}, then the matrix in this step can be given by:

$$H_{row} = kron\left[kron\left(I_2, I_2^{\otimes n}\right), H_{2^n}\right] = I_2 \otimes I_2^{\otimes n} \otimes H_{2^n} \tag{14}$$

where the function *kron( )* represents the tensor product operation of two matrices.

Step 2 (Column Decomposition): Similar to step 1, column decomposition is by applying the H_{2^n} matrix on the FRQI image's coordinate qubits $|Y\rangle = |y_{n-1}y_{n-2}\cdots y_1y_0\rangle$ in the vertical direction, and if the corresponding matrix is H_{column}, then it can be written as:

$$H_{column} = kron\left[kron\left(I_2, H_{2^n}\right), I_2^{\otimes n}\right] = I_2 \otimes H_{2^n} \otimes I_2^{\otimes n} \tag{15}$$

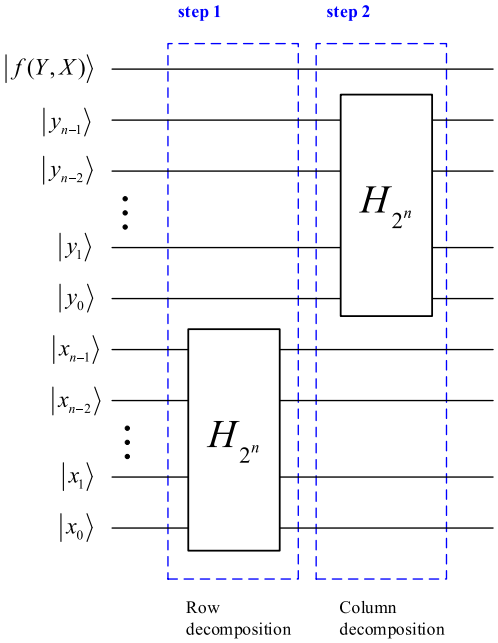

FIGURE 8. Effective circuit of full levels decomposition for FRQI image based on standard QHWT transformation.

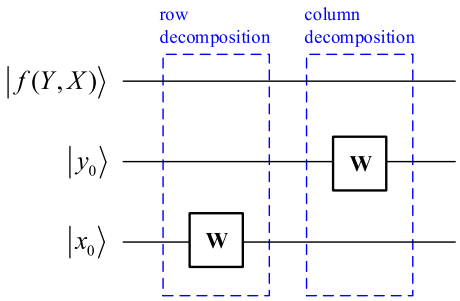

FIGURE 9. Quantum circuit for a 2 × 2 FRQI image decomposition based on QHWT.

Therefore, the quantum matrix for an FRQI image decomposition based on QHWT can be expressed as:

$$H = H_{column}H_{row} = \left(I_2 \otimes H_{2^n} \otimes I_2^{\otimes n}\right)\left(I_2 \otimes I_2^{\otimes n} \otimes H_{2^n}\right) \tag{16}$$

To provide an intuition of how to decompose a FRQI image based on QHWT, Fig. 9 shows an example of the quantum circuit for a 2 × 2 FRQI image decomposition.

As shown in Fig. 4, the 2 × 2 FRQI image can be written as:

$$\begin{aligned} |I\rangle = & \frac{1}{2}\left[\left(\cos\theta_0\,|0\rangle + \sin\theta_0\,|1\rangle\right)|00\rangle\right. \\ & + \left(\cos\theta_1\,|0\rangle + \sin\theta_1\,|0\rangle\right)|01\rangle \\ & + \left(\cos\theta_2\,|0\rangle + \sin\theta_2\,|1\rangle\right)|10\rangle \\ & \left. + \left(\cos\theta_3\,|0\rangle + \sin\theta_3\,|1\rangle\right)|11\rangle\right] \\ = & \frac{1}{2}\left[\cos\theta_0 \quad \cos\theta_1 \quad \cos\theta_2 \quad \cos\theta_3\right. \\ & \left.\sin\theta_0 \quad \sin\theta_1 \quad \sin\theta_2 \quad \sin\theta_3\right]^T \end{aligned} \tag{17}$$

$$H = H_{column} H_{row} = (I_2 \otimes W \otimes I_2)(I_2 \otimes I_2 \otimes W)$$
$$= \begin{bmatrix} \frac{1}{\sqrt{2^2}} & \frac{1}{\sqrt{2^2}} & \frac{1}{\sqrt{2^2}} & \frac{1}{\sqrt{2^2}} & 0 & 0 & 0 & 0 \\ \frac{1}{\sqrt{2^2}} & -\frac{1}{\sqrt{2^2}} & \frac{1}{\sqrt{2^2}} & -\frac{1}{\sqrt{2^2}} & 0 & 0 & 0 & 0 \\ \frac{1}{\sqrt{2^2}} & \frac{1}{\sqrt{2^2}} & -\frac{1}{\sqrt{2^2}} & -\frac{1}{\sqrt{2^2}} & 0 & 0 & 0 & 0 \\ \frac{1}{\sqrt{2^2}} & -\frac{1}{\sqrt{2^2}} & -\frac{1}{\sqrt{2^2}} & \frac{1}{\sqrt{2^2}} & 0 & 0 & 0 & 0 \\ 0 & 0 & 0 & 0 & \frac{1}{\sqrt{2^2}} & \frac{1}{\sqrt{2^2}} & \frac{1}{\sqrt{2^2}} & \frac{1}{\sqrt{2^2}} \\ 0 & 0 & 0 & 0 & \frac{1}{\sqrt{2^2}} & -\frac{1}{\sqrt{2^2}} & \frac{1}{\sqrt{2^2}} & -\frac{1}{\sqrt{2^2}} \\ 0 & 0 & 0 & 0 & \frac{1}{\sqrt{2^2}} & \frac{1}{\sqrt{2^2}} & -\frac{1}{\sqrt{2^2}} & -\frac{1}{\sqrt{2^2}} \\ 0 & 0 & 0 & 0 & \frac{1}{\sqrt{2^2}} & -\frac{1}{\sqrt{2^2}} & -\frac{1}{\sqrt{2^2}} & \frac{1}{\sqrt{2^2}} \end{bmatrix} \tag{18}$$

Based on equations (16) and (12), it is easy to deduce that the matrix expression of QHWT for a 2×2 FRQI can be expressed as, (18) shown at the top of this page.

Therefore, the quantum transformation for the 2×2 FRQI image decomposition based on QHWT is given by:

$$H(|I\rangle) = \frac{1}{2\sqrt{2^2}} \begin{bmatrix} \cos\theta_0 + \cos\theta_1 + \cos\theta_2 + \cos\theta_3 \\ \cos\theta_0 - \cos\theta_1 + \cos\theta_2 - \cos\theta_3 \\ \cos\theta_0 + \cos\theta_1 - \cos\theta_2 - \cos\theta_3 \\ \cos\theta_0 - \cos\theta_1 - \cos\theta_2 + \cos\theta_3 \\ \sin\theta_0 + \sin\theta_1 + \sin\theta_2 + \sin\theta_3 \\ \sin\theta_0 - \sin\theta_1 + \sin\theta_2 - \sin\theta_3 \\ \sin\theta_0 + \sin\theta_1 - \sin\theta_2 - \sin\theta_3 \\ \sin\theta_0 - \sin\theta_1 - \sin\theta_2 + \sin\theta_3 \end{bmatrix}$$
$$= \frac{1}{2} \Bigg\{ \underbrace{\frac{1}{2} \begin{bmatrix} (\cos\theta_0 + \cos\theta_1 + \cos\theta_2 + \cos\theta_3)|0\rangle \\ +(\sin\theta_0 + \sin\theta_1 + \sin\theta_2 + \sin\theta_3)|1\rangle \end{bmatrix}}_{\text{color information}} |00\rangle$$
$$+ \underbrace{\frac{1}{2} \begin{bmatrix} (\cos\theta_0 - \cos\theta_1 + \cos\theta_2 - \cos\theta_3)|0\rangle \\ +(\sin\theta_0 - \sin\theta_1 + \sin\theta_2 - \sin\theta_3)|1\rangle \end{bmatrix}}_{\text{color information}} |01\rangle$$
$$+ \underbrace{\frac{1}{2} \begin{bmatrix} (\cos\theta_0 + \cos\theta_1 - \cos\theta_2 - \cos\theta_3)|0\rangle \\ +(\sin\theta_0 + \sin\theta_1 - \sin\theta_2 - \sin\theta_3)|1\rangle \end{bmatrix}}_{\text{color information}} |10\rangle$$
$$+ \underbrace{\frac{1}{2} \begin{bmatrix} (\cos\theta_0 - \cos\theta_1 - \cos\theta_2 + \cos\theta_3)|0\rangle \\ +(\sin\theta_0 - \sin\theta_1 - \sin\theta_2 + \sin\theta_3)|1\rangle \end{bmatrix}}_{\text{color information}} |11\rangle \Bigg\} \tag{19}$$

where color information in position $|00\rangle$ denotes the approximation, and color information in position $|01\rangle$, $|10\rangle$, and $|11\rangle$ represents the horizontal detail information, vertical detail information, and diagonal detail information, respectively.

V. QUANTUM IMAGE WATERMARKING

Two different quantum watermark image embedding algorithms are proposed to embed a $2^{n-1} \times 2^{n-1}$ binary watermark image into a $2^n \times 2^n$ grayscale carrier image, namely non-block and block quantum watermarking schemes. The quantum watermark image embedding and extracting algorithms as well as their effective circuits are illustrated in detail in this section.

A. NON-BLOCK AND BLOCK 1ST-LEVEL DECOMPOSITION

Assume the quantum carrier image is a $2^n \times 2^n$ grayscale image $|C\rangle$ as given in (13). Based on full-level quantum circuit for QHWT transformation demonstrated in Fig. 7, the quantum circuits of non-block and block 1st-level based decomposition for an FRQI image are illustrated in Fig. 10 and Fig. 11, respectively.

As shown in Fig. 10 and Fig. 11, non-block and block 1st-level decomposition of the FRQI images are both realized through two stages: row decomposition and column decomposition. Therefore, we can deduce the following matrices for non-block and block 1st-level decomposition.

$$\begin{aligned} non-block: \quad & \left(I_2 \otimes \Pi_{2^n} \otimes I_2^{\otimes n}\right)\left(I_2^{\otimes n} \otimes W \otimes I_2^{\otimes n}\right) \\ & \times \left(I_2^{\otimes n+1} \otimes \Pi_{2^n}\right)\left(I_2^{\otimes 2n} \otimes W\right) \\ block: \quad & \left(I_2^{\otimes n-2} \otimes \Pi_8 \otimes I_2^{\otimes n}\right)\left(I_2^{\otimes n} \otimes W \otimes I_2^{\otimes n}\right) \\ & \times \left(I_2^{\otimes 2n2} \otimes \Pi_8\right)\left(I_2^{\otimes 2n} \otimes W\right) \end{aligned} \tag{20}$$

For non-block 1st-level decomposition, the image is divided into four parts: approximation, horizontal detail, vertical detail, and diagonal detail. Each part has a size of $2^{n-1} \times 2^{n-1}$.

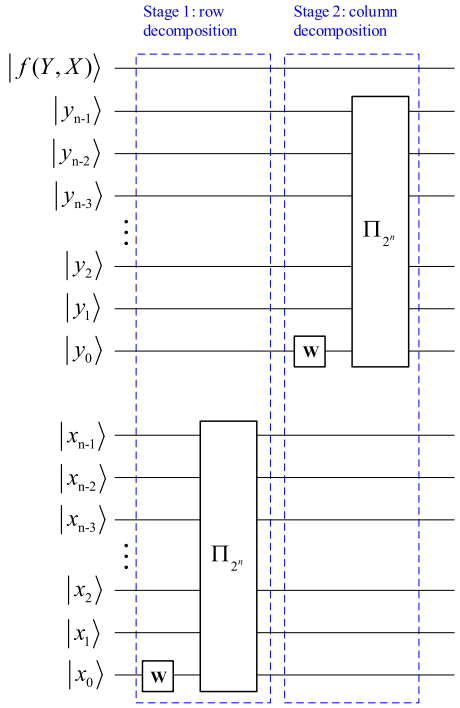

FIGURE 10. Quantum circuit of non-block 1st-level decomposition for FRQI image.

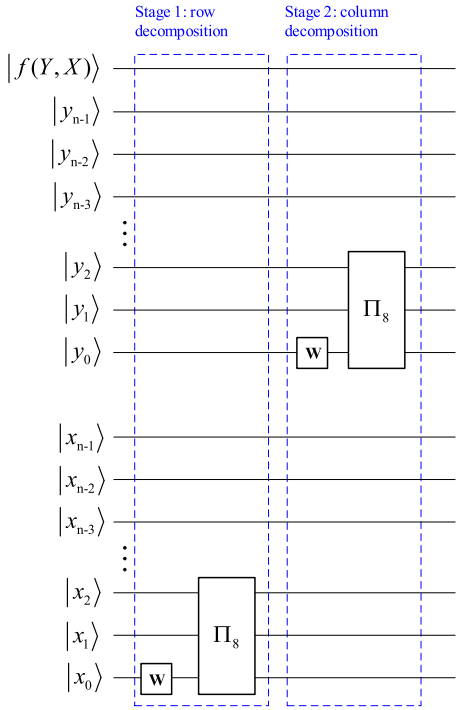

FIGURE 11. Quantum circuit of block 1st-level decomposition for FRQI image.

In the case of block decomposition, the entire image is divided into $2^{n-3} \times 2^{n-3}$ blocks with a block size of 8×8. Each block consists of the same four parts as mentioned above, where each part has a size of 4×4. Figure 12 demonstrates the subband graphs of non-block and block 1st-level decomposition based on QHWT.

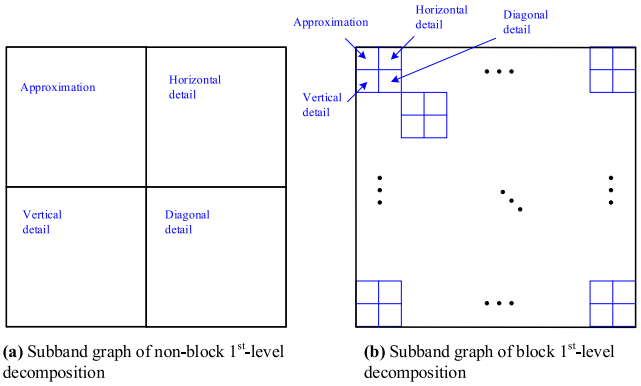

(a) Subband graph of non-block 1st-level decomposition

(b) Subband graph of block 1st-level decomposition

FIGURE 12. Subband graphs of non-block (a) and block (b) 1st-level decomposition.

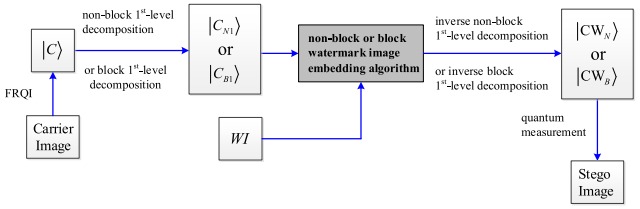

FIGURE 13. Non-block and block quantum watermark image embedding procedures.

Note that the approximation subband, having the low frequency content, coarsely describes the image and contains much of the energy of the original image. The higher frequency coefficients in the detailed subbands represent the fine details of the image and their energy is relatively small compared to the approximation subband. Specifically, since the wavelet coefficients and variances of the edge sub-images represented by horizontal and vertical detail are commonly greater than diagonal details, the diagonal subband is selected for watermark information insertion as it has a less important role in image reconstruction process.

B. QUANTUM WATERMARK IMAGE EMBEDDING

Based on non-block and block 1st-level decomposition, the procedures for non-block and block quantum watermark image embedding are summarized in Fig. 13.

1) NON-BLOCK QUANTUM WATERMARK IMAGE EMBEDDING ALGORITHM AND CIRCUIT DESIGN

Since the watermark image information is known, we can assume the binary watermark image WI with a size of $2^{n-1} \times 2^{n-1}$ has the following form:

$$WI = \sum_{Y=0}^{2^{n-1}-1} \sum_{X=0}^{2^{n-1}-1} f(Y,X),$$
$$Y = y_{n-2}y_{n-3}\cdots y_1y_0, \quad X = x_{n-2}x_{n-3}\cdots x_1x_0,$$
$$f(Y,X) \in \{0,1\}, \quad y_i,\ x_i \in \{0,1\},$$
$$i = 0, 1, 2, \cdots, n-2 \tag{21}$$

Then, based on the pixel value *f(Y, X)* in each position *(Y, X)*, we can define the unitary matrix $R_y(2\varphi_K)$ as follows:

$$R_y(2\varphi_K) = \begin{bmatrix} \cos(\varphi_K) & -\sin(\varphi_K) \\ \sin(\varphi_K) & \cos(\varphi_K) \end{bmatrix},$$
$$\varphi_K = 0, \quad \frac{5 \times \pi}{2 \times 255} \tag{22}$$

where $\varphi_K = 0$ and $\varphi_K = \frac{5\times\pi}{2\times255}$ are associated with the pixel information $f(Y, X) = 0$ and $f(Y, X) = 1$ of binary image *WI*, respectively. $K = YX = 0, 1, 2, \cdots, 2^{2n-2} - 1$ denote the pixel location information in the watermark image *WI*.

Based on the above preparation, the non-block quantum watermark image embedding algorithm has the following steps:

Step 1: The quantum carrier image is decomposed using the non-block 1st-level QHWT, shown in Fig. 10, which results in the middle quantum state $|C_{N1}\rangle$ given by:

$$|C_{N1}\rangle = \left(I_2 \otimes \Pi_{2^n} \otimes I_2^{\otimes n}\right)\left(I_2^{\otimes n} \otimes W \otimes I_2^{\otimes n}\right) \times \left(I_2^{\otimes n+1} \otimes \Pi_{2^n}\right)\left(I_2^{\otimes 2n} \otimes W\right)|C\rangle \tag{23}$$

where the middle quantum state $|C_{N1}\rangle$ is divided into four parts: approximation, horizontal detail, vertical detail, and diagonal detail information as shown in Fig. 12(a).

Step 2: Based on the unitary matrix $R_y(2\varphi_K)$, we can design the multiple qubits control unitary transforms U_K^C. The unitary operator U_K^E is constructed from U_K^C and applied to the diagonal detail information within the middle quantum state $|C_{N1}\rangle$ as follows:

$$U_K^C = R_y(2\varphi_K) \otimes |Y\rangle|X\rangle\langle X|\langle Y|$$
$$|CN\rangle = U_K^E|C_{N1}\rangle = \left(\prod_{K=0}^{2^{2n-2}-1} U_K^C\right)|C_{N1}\rangle \tag{24}$$

where $|Y\rangle = |y_{n-1}y_{y-2}\cdots y_1y_0\rangle$ and $|X\rangle = |y_{n-1}x_{n-2}\cdots x_1x_0\rangle$ have the highest qubits $|y_{n-1}\rangle = |1\rangle$ and $|x_{n-1}\rangle = |1\rangle$. The area of the diagonal detail of the middle quantum state $|y_{n-1}\rangle = |1\rangle$ can be selected by restricting the highest qubits to $|y_{n-1}\rangle = |1\rangle$ and $|x_{n-1}\rangle = |1\rangle$. Therefore, through the quantum operator U_K^E, the pixel information of the watermark image is inserted into the diagonal wavelet coefficients of the carrier image. In other words, when the pixel value of the watermark image is bit 0, the corresponding diagonal wavelet coefficients is left unchanged. On the other hand, when the pixel bit of the watermark image is 1, a slight change is introduced to the corresponding diagonal wavelet coefficients via multi-qubit controlled unitary $R_y(2\varphi_K)$ gate.

Step 3: The watermarked image $|CW_N\rangle$ is reconstructed by computing the inverse non-block 1st-level transform of the quantum state $|CN\rangle$. The unitary matrices can be expressed as:

$$|CW_N\rangle = \left[\left(I_2^{\otimes n+1} \otimes \Pi_{2^n}\right)\left(I_2^{\otimes 2n} \otimes W\right)\right]^\dagger \left[\left(I_2 \otimes \Pi_{2^n} \otimes I_2^{\otimes n}\right)\left(I_2^{\otimes n} \otimes W \otimes I_2^{\otimes n}\right)\right]^\dagger |CN\rangle \tag{25}$$

where $[]^\dagger$ denotes the Hermite conjugate matrix.

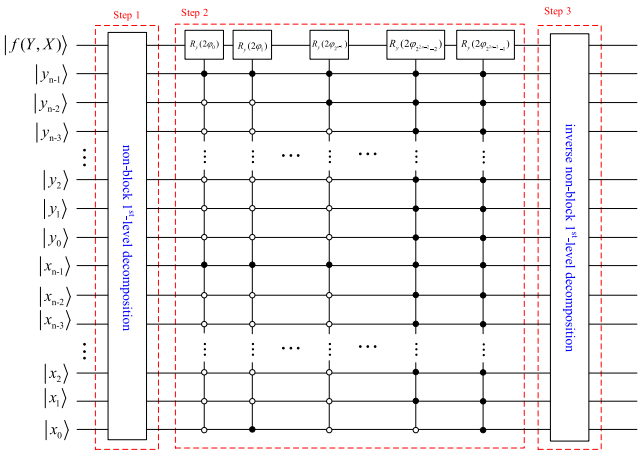

FIGURE 14. Circuit for non-block quantum watermark image embedding process.

Step 4: The quantum measurement is utilized for the states in superposition to collapse to final states to obtain the classical Stego image.

Based on description above, the integrated quantum circuit for non-block quantum watermark image embedding (from Step 1 to Step 3) is demonstrated in Fig. 14.

2) BLOCK QUANTUM WATERMARK IMAGE EMBEDDING ALGORITHM AND CIRCUIT DESIGN

The non-block watermarking embedding approach inserts the watermark image information into the diagonal wavelet coefficients of the whole quantum carrier image based on the non-block 1st-level decomposition of QHWT. In this subsection, the watermark image information is embedded into the carrier image using the block quantum watermarking embedding scheme. In this method, the watermark image information is scattered and embedded into blocks of the carrier image based on block 1st-level decomposition of QHWT.

The FRQI image representation model provides an easy method to partition an image into blocks. A block can be selected by restricting the location indices to a specific range. To achieve this objective, we can split the qubits $|Y\rangle = |y_{n-1}\cdots y_3y_2y_1y_0\rangle$ and $|X\rangle = |x_{n-1}\cdots x_3x_2x_1x_0\rangle$ of the quantum carrier image $|C\rangle$ into the following two parts:

$$|Y\rangle = |Y_{n-3}\rangle|Y_3\rangle = |y_{n-1}\cdots y_3\rangle|y_2y_1y_0\rangle$$
$$|X\rangle = |X_{n-3}\rangle|X_3\rangle = |x_{n-1}\cdots x_3\rangle|x_2x_1x_0\rangle \tag{26}$$

where qubits $|Y_{n-3}\rangle = |y_{n-1}\cdots y_3\rangle$ and $|X_{n-3}\rangle = |x_{n-1}\cdots x_3\rangle$ are called inter-block coordinates. The remaining qubits $|Y_3\rangle = |y_2y_1y_0\rangle$ and $|X_3\rangle = |x_2x_1x_0\rangle$ are called the intra-block coordinates as they correspond to the specific locations within blocks. Therefore, by splitting the coordinate qubits into two parts as defined in (26), the $2^n \times 2^n$ quantum carrier image $|C\rangle$ is divided into $2^{n-3} \times 2^{n-3}$ blocks with block size of $2^3 \times 2^3$.

Similarly, based on the known watermark image *WI* expressed in (21), we can also split the location information $Y = y_{n-2}\cdots y_3y_2y_1y_0$ and $X = x_{n-2}\cdots x_2x_1x_0$ of *WI* into

two parts as follows:

$$\begin{aligned} Y &= Y_{n-3}, \quad Y_2 = y_{n-2}\cdots y_3 y_2,\ y_1 y_0 \\ X &= X_{n-3}, \quad X_2 = x_{n-2}\cdots x_3 x_2,\ x_1 x_0 \end{aligned} \tag{27}$$

Therefore, the watermark image WI is also divided into $2^{n-3} \times 2^{n-3}$ blocks with block size of $2^2 \times 2^2$. Herein, the coordinates of $Y_{n-3} = y_{n-2}\cdots y_3 y_2$ and $X_{n-3} = x_{n-2}\cdots x_3 x_2$ are also called inter-block coordinates. The remaining location information represented by $Y_2 = y_1 y_0$ and $X_2 = x_1 x_0$ is called the intra-block coordinates because they correspond to the pixel locations within blocks.

After introducing how to divide the quantum carrier image $|C\rangle$ and watermark image WI into blocks, the block watermark image embedding algorithm can be summarized as follows:

Step 1: Implement block 1st-level decomposition based on QHWT for the carrier image $|C\rangle$ to obtain the middle quantum state $|C_{B1}\rangle$. The circuit is shown in Fig. 11 and its unitary matrix can be written as:

$$\begin{aligned} |C_{B1}\rangle = &\left(I_2^{\otimes n-2} \otimes \Pi_8 \otimes I_2^{\otimes n}\right)\left(I_2^{\otimes n} \otimes W \otimes I_2^{\otimes n}\right) \\ &\times \left(I_2^{\otimes 2n-2} \otimes \Pi_8\right)\left(I_2^{\otimes 2n} \otimes W\right)|C\rangle \end{aligned} \tag{28}$$

If S_k denotes the K^{th} block in the middle quantum state $|C_{B1}\rangle$, S_k can be calculated as:

$$\begin{aligned} S_k = &\ y_{n-1} \times 2^{2n-7} + y_{n-2} \times 2^{2n-8} + \cdots + y_3 \times 2^{n-3} \\ &+ x_{n-1} \times 2^{n-4} + x_{n-2} \times 2^{n-5} + \cdots + x_3 \times 2^0 \end{aligned} \tag{29}$$

Similarly, if we also use S_k to denote the K^{th} block in the watermark image WI, S_k can be calculated as:

$$\begin{aligned} S_k = &\ y_{n-2} \times 2^{2n-7} + y_{n-3} \times 2^{2n-8} + \cdots + y_2 \times 2^{n-3} \\ &+ x_{n-2} \times 2^{n-4} + x_{n-3} \times 2^{n-5} + \cdots + x_2 \times 2^0 \end{aligned} \tag{30}$$

Each $2^2 \times 2^2$ block of the watermark image contains sixteen pixels. Therefore, based on the pixel value $f(Y, X)$ in position (Y, X) of each block, we can define the sixteen unitary matrices $R_y(2\varphi_K)$ as follows:

$$\begin{aligned} R_y(2\varphi_K) = &\begin{bmatrix} \cos(\varphi_K) & -\sin(\varphi_K) \\ \sin(\varphi_K) & \cos(\varphi_K) \end{bmatrix}, \quad \varphi_K = 0, \quad \frac{5\times\pi}{2\times 255} \\ K = &\ (S_k - 1) \times 2^4, \quad (S_k - 1) \times 2^4 + 1, \cdots, \\ &\times (S_k - 1) \times 2^4 + 14, \quad S_k \times 2^4 - 1 \end{aligned} \tag{31}$$

where $K = y_1 y_0 x_1 x_0$ denotes the pixel location information in each block of the watermark image WI. $\varphi_K = 0$ and $\varphi_K = \frac{5\times\pi}{2\times 255}$ are also associated with the pixel information $f(Y, X) = 0$ and $f(Y, X) = 1$ of the binary watermark image WI, respectively.

Step 2: After the block 1st-level decomposition, the middle quantum state $|C_{B1}\rangle$ is divided into $2^{n-3} \times 2^{n-3}$ blocks with block size of $2^3 \times 2^3$. Each block consists of four parts: approximation, horizontal detail, vertical detail, and diagonal detail information with a size of $2^2 \times 2^2$ as shown in Fig. 12(b).

Each block S_k in the middle quantum state $|C_{B1}\rangle$ contains sixteen diagonal wavelet coefficients. To embed the watermark image information into the carrier image, sixteen specific multiple qubits control unitary transformations $R_y\left(2\varphi_{(S_k-1)\times 2^4}\right)$, $R_y\left(2\varphi_{(S_k-1)\times 2^4+1}\right), \cdots, R_y\left(2\varphi_{S_k\times 2^4-2}\right)$, $R_y\left(2\varphi_{S_k\times 2^4-1}\right)$ as defined in (31) are used to construct the quantum unitary operators U_K^C and U_K^E in each block S_k as given by the following equations:

$$\begin{aligned} U_K^C = &\ R_y(2\varphi_K) \otimes \sum_{YX=K}^{2^{2n-2}-1} |1\rangle|Y\rangle|1\rangle|X\rangle\langle X|\langle 1|\langle Y|\langle 1| \\ K = &\ (S_k - 1) \times 2^4, \quad (S_k - 1) \times 2^4 + 1, \ldots, S_k \times 2^4 - 2, \\ &\times S_k \times 2^4 - 1 \\ Y = &\ y_{n-2} y_{n-3} \cdots y_1 y_0, \quad X = x_{n-2} x_{n-3} \cdots x_1 x_0 \\ |CB\rangle = U_K^E |C_{B1}\rangle = &\left(\prod_{K=(S_k-1)\times 2^4}^{S_k\times 2^4-1} U_K^C\right)|C_{B1}\rangle \end{aligned} \tag{32}$$

where the subscript K is the index of the unitary operations performed on the S_k block within the quantum middle state $|C_{B1}\rangle$.

Therefore, through a series of applications of the quantum operators U_K^E to each block, the pixel information of the watermark image WI within each block is inserted into the diagonal wavelet coefficients of the quantum carrier image $|C\rangle$.

Step 3: The inverse block 1st-level transform of the quantum state $|CB\rangle$ is used to obtain the watermarked image $|CW_B\rangle$. The corresponding matrix expression in this step is given by:

$$\begin{aligned} |CW_B\rangle = &\left[\left(I_2^{\otimes 2n-2} \otimes \Pi_8\right)\left(I_2^{\otimes 2n} \otimes W\right)\right]^\dagger \\ &\left[\left(I_2^{\otimes n-2} \otimes \Pi_8 \otimes I_2^{\otimes n}\right)\left(I_2^{\otimes n} \otimes W \otimes I_2^{\otimes n}\right)\right]^\dagger |CB\rangle \end{aligned} \tag{33}$$

Step 4: The Stego image in the classical domain is obtained from the quantum watermarked image by quantum measurements.

The complete integrated quantum circuit (from Step 1 to Step 3) for the whole image containing all of the blocks is very large and complex. Therefore, it is more convenient to only show the circuit for a single block embedding which is demonstrated in Fig. 15.

C. QUANTUM WATERMARK IMAGE EXTRACTION

The non-block and block quantum watermarking algorithms both introduce small changes to the diagonal wavelet coefficients of the quantum carrier image. Therefore, it is a non-blind watermarking scheme, which means that the original carrier image C and the Stego image CW are necessary to retrieve the watermark image information. Figure 16 gives the detailed procedures for non-block and block watermark image extraction.

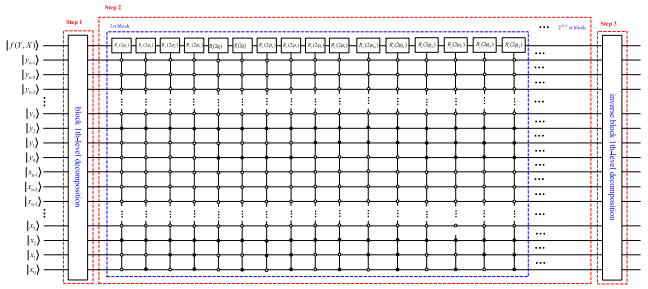

FIGURE 15. Circuit for a single block quantum watermark image embedding.

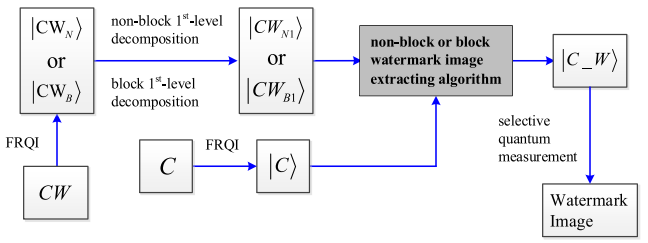

FIGURE 16. Non-block and block quantum watermark image extraction procedures.

1) NON-BLOCK QUANTUM WATERMARK IMAGE EXTRACTION ALGORITHM AND CIRCUIT DESIGN

Based on the quantum carrier image $|C\rangle$, we can implement non-block decomposition to obtain the diagonal wavelet coefficients in frequency domain. On condition that qubits $|y_{n-1}\rangle = |1\rangle$ and $|x_{x-1}\rangle = |1\rangle$ of the quantum carrier image $|CW_{N1}\rangle$. Suppose the diagonal wavelet coefficients are denoted by d_i, $i = 0, 1, 2, \cdots, 2^{2n-2} - 1$, where the subscript i is the index indicating the location information within diagonal wavelet coefficients. $|i\rangle = |y_{n-2}y_{n-3}\cdots y_1y_0\rangle\,|x_{n-2}x_{n-3}\cdots x_1\,x_0\rangle$, and the decimal number i can be calculated as follows:

$$\begin{aligned} i = {} & y_{n-2}\times 2^{2n-3} + y_{n-3}\times 2^{2n-4} + \cdots + y_1\times 2^{n} + y_0\times 2^{n-1} \\ & + x_{n-2}\times 2^{n-2} + x_{n-3}\times 2^{n-3} + \cdots + x_1\times 2^{1} + x_0\times 2^{0} \end{aligned} \quad (34)$$

Based on the diagonal wavelet coefficients, let the sequence of angles φ_0, φ_1, $\varphi_2, \cdots, \varphi_{2^{2n-2}-2}$, $\varphi_{2^{2n-2}-1}$ correspond to the diagonal wavelet coefficients d_0, d_1, $d_2, \cdots, d_{2^{2n-2}-2}$, $d_{2^{2n-2}-1}$, where $\varphi_i = ar\cos(d_i)$, $i = 0, 1, 2, \cdots, 2^{2n-2} - 1$, and the arcos function is the inverse cosine function. Therefore, a series of rotation gates $C(2\varphi_i)$ are defined based on the computed angles as follows:

$$C(2\varphi_i) = \begin{bmatrix} \cos\varphi_i & \sin\varphi_i \\ \sin\varphi_i & -\cos\varphi_i \end{bmatrix}, \quad i = 0, 1, 2, \cdots, 2^{2n-2} - 2, \quad 2^{2n-2} - 1 \quad (35)$$

Therefore, the result of subsequently applying the Z gate and the rotation gate $C(2\varphi_i)$ on a single qubit $|\psi\rangle = \cos\theta\,|0\rangle + \sin\theta\,|1\rangle$ can be described as follows:

$$\begin{aligned} Z\left(C(2\varphi_i)\,|\psi\rangle\right) &= Z\left(\cos(\varphi_i - \theta)\,|0\rangle + \sin(\varphi_i - \theta)\,|1\rangle\right) \\ &= \cos(\theta - \varphi_i)\,|0\rangle + \sin(\theta - \varphi_i)\,|0\rangle \end{aligned} \quad (36)$$

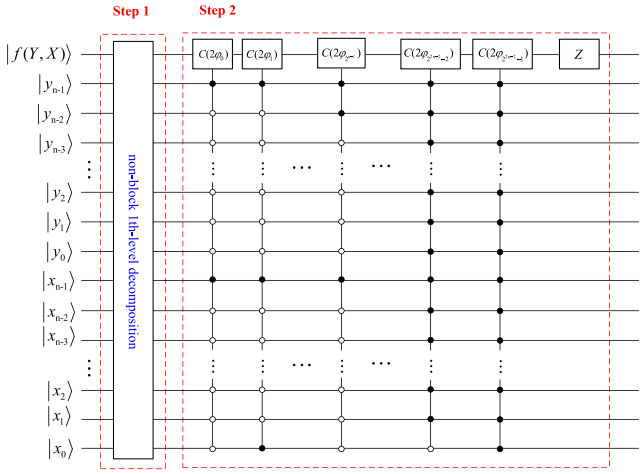

FIGURE 17. Effective circuit for non-block watermark image extraction.

Based on the above analysis, the following steps are used to realize the non-block quantum watermark image extraction algorithm.

Step 1: Stego image $|CW_N\rangle$ is decomposed using the non-block 1st-level transform to obtain the middle quantum state $|CW_{N1}\rangle$.

Step 2: A sequence of multiple qubits controlled unitary operators U_K^T and the Z gate is constructed and applied to the middle quantum state $|CW_{N1}\rangle$ as follows:

$$\begin{aligned} U_K^T &= C(2\varphi_K) \otimes |1\rangle\,|Y\rangle\,|1\rangle\,|X\rangle\,\langle X|\,\langle 1|\,\langle Y|\,\langle 1| \\ |K\rangle &= |Y\rangle\,|X\rangle \\ |Y\rangle &= |y_{n-2}y_{n-3}\cdots y_1y_0\rangle\,, \quad |X\rangle = |x_{n-2}x_{n-3}\cdots x_1x_0\rangle \\ |C\_W\rangle &= Z\left(U\,|CW_{N1}\rangle\right) = Z\left[\left(\prod_{K=0}^{2^{2n-2}-1} U_K^T\right)|CW_{N1}\rangle\right] \end{aligned} \quad (37)$$

The effective circuit for non-block watermark image extraction is shown in Fig. 17. Finally, selective quantum measurement operations are utilized to retrieve the watermark image information, i.e., measure the diagonal wavelet coefficients. Theoretically, if the quantum measurement result is quantum state $|0\rangle$ with a probability of 100%, the extracted watermark image bit is 0; otherwise, the extracted watermark image bit is 1.

2) BLOCK QUANTUM WATERMARK IMAGE EXTRACTION ALGORITHM AND CIRCUIT DESIGN

Similar to the non-block watermark image extracting procedure, the block 1st-level transform will be used to decompose the original carrier image $|C\rangle$, and obtain the corresponding sixteen diagonal wavelet coefficients within each block in frequency domain. Assume that these coefficients in the S_k block are $d_{(S_k-1)\times 2^4}$, $d_{(S_k-1)\times 2^4+1}$, $d_{(S_k-1)\times 2^4+2}, \cdots, d_{S_k\times 2^4-2}$, $d_{S_k\times 2^4-1}$ in order, where S_k can be calculated by (29). Therefore, in each block, the associated sixteen angles $\varphi_{(S_k-1)\times 2^4}$, $\varphi_{(S_k-1)\times 2^4+1}$, $\varphi_{(S_k-1)\times 2^4+2}, \cdots, \varphi_{S_k\times 2^4-2}$, $\varphi_{S_k\times 2^4-1}$ are

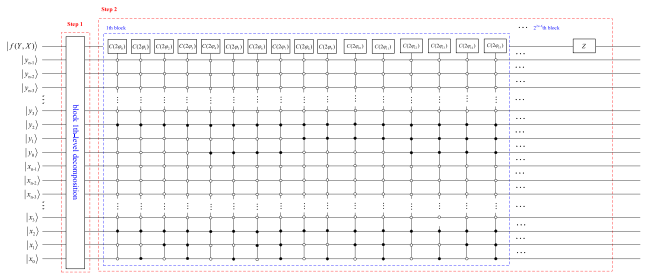

FIGURE 18. Effective circuit for a single block watermark image extraction.

obtained via the inverse cosine function, where $\varphi_i = \arccos(d_i)$, $i = (S_k - 1) \times 2^4, (S_k - 1) \times 2^4 + 1, \cdots, S_k \times 2^4 - 2, S_k \times 2^4 - 1$.

Based on these angles in each block, we can also define the following series of unitary rotation matrices $C(2\varphi_i)$:

$$\begin{aligned} C(2\varphi_i) &= \begin{bmatrix} \cos\varphi_i & \sin\varphi_i \\ \sin\varphi_i & -\cos\varphi_i \end{bmatrix} \\ i &= (S_k - 1) \times 2^4, \quad (S_k - 1) \times 2^4 + 1, \\ &\quad \times (S_k - 1) \times 2^4 + 2, \cdots, S_k \times 2^4 - 2, \\ &\quad \times S_k \times 2^4 - 1 \end{aligned} \tag{38}$$

For simplicity, the integrated circuit for a single block quantum watermark image extraction is demonstrated in Fig. 18. The algorithm consists of the following two steps:

Step 1: The individual blocks of the Stego image $|CW_B\rangle$ are decomposed by block 1st-level transform to obtain the middle quantum state $|CW_{B1}\rangle$.

Step 2: A sequence of multiple qubits controlled unitary operators U_i^T and the Z gate in each block operate on the middle quantum state $|CW_{B1}\rangle$ to compute $|C\_W\rangle$:

$$\begin{aligned} U_i^T &= C(2\varphi_i) \otimes |Y\rangle |X\rangle \langle X| \langle Y| \\ |C\_W\rangle &= Z\left(U |CW_{B1}\rangle\right) = Z\left[\left(\prod_{i=(S_k-1)\times 2^4}^{S_k\times 2^4-1} U_i^T\right) |CW_{B1}\rangle\right] \end{aligned} \tag{39}$$

where the quantum operator U denotes the unitary operations applied on the K^{th} block.

Finally, to retrieve the watermark image information, we must implement selective quantum measurement operations in each block, i.e., measure the diagonal wavelet coefficients within each block. The principle of retrieving the watermark image information from the quantum registers is similar to the non-block watermark image extraction process.

D. QUANTUM MEASUREMENT

To determine the classical image information from the quantum registers, a measurement of the quantum state based on multi-projection operators is incorporated. For the FRQI images expressed in (3), the image retrieval process can be explained by the following two steps:

Step 1: Apply the observable operator M_1

$$M_1 = \sum_{i=0}^{2^{2n}-1} I \otimes m_i |i\rangle \langle i| \tag{40}$$

to the last 2n-qubit of the FRQI image $|I(\theta)\rangle$. Then, the quantum images' superposition state would collapse into the basis state $(\cos\theta_i |0\rangle + \sin\theta_i |1\rangle) |i\rangle$ with a probability of $1/2^{2n}$.

Step 2: Use the observable measurement operator M_2

$$M_2 = \sum_{i=0}^{1} m_i |i\rangle \langle i| = m_0 |0\rangle \langle 0| + m_1 |1\rangle \langle 1| \tag{41}$$

to measure the pixel information of $\cos\theta_i |0\rangle + \sin\theta_i |1\rangle$. As a result, obtain qubit $|0\rangle$ with a probability of $\cos^2\theta_{YX}$ or qubit $|1\rangle$ with a probability of $\sin^2\theta_{YX}$. Consequently, $\theta_{YX} = \arccos\left(\sqrt{\cos^2\theta_{YX}}\right) = \arcsin\left(\sqrt{\sin^2\theta_{YX}}\right)$ can be directly obtained.

Note that the quantum information of FRQI images is encoded into a superposition state in quantum registers. Therefore, when measuring the quantum registers to determine the pixel color information, the quantum registers will collapse into one of the computational basis states of the corresponding quantum superposition state. Due to the probabilistic nature of quantum registers, it is highly unlikely to obtain all of the pixel information in an image by only using a one-time quantum measurement operation. Therefore, the measurement operations need to be repeated many times to retrieve all of the image information [12], [41]. This converts the probabilistic quantum information into the deterministic classical domain in the form of probability distributions. By extracting and analyzing these distributions, the corresponding classical image information is obtained.

E. COMPLEXITY ANALYSIS

In quantum computation, any complex quantum circuit can be decomposed into a succession of basic unitary gates that only act on one or two qubits [3], [38]. In this paper, we consider one-qubit or two-qubit quantum gates as the basic units for computing the algorithm complexity. Therefore, the integrated quantum circuit complexity depends on the number of these elementary gates. In addition, it is a common approach that introduces the ancillary qubits when decomposing the complex quantum unitary operations into a series of basic quantum gates [3].

Suppose the sizes of the quantum carrier and watermark images are $2^n \times 2^n$ and $2^{n-1} \times 2^{n-1}$, respectively. The circuit complexity of the presented quantum image watermarking schemes demonstrated in Figs. 14, 15, 17 and 18 can be computed in terms of n as discussed in the remainder of this subsection.

As shown in Fig. 14, the circuit for the non-block quantum watermark image embedding scheme is divided into three operations: (1) non-block 1st-level decomposition using QHWT; (2) a sequence of multi-qubit controlled rotation operations; (3) and inverse non-block 1st-level transform.

Therefore, the quantum circuit complexity can be analyzed and calculated from the aforementioned three main operations as follows:

Operation 1: The non-block 1st-level transform has the quantum circuit shown in Fig. 10, which contains two W gates and two permutation operators Π_{2^n}. The quantum circuit for Π_{2^n}, illustrated in Fig. 6, consists of (n-1) swap gates. Thus, the circuit complexity of the first operation is $2 + 2(n-1) = 2n$.

Operation 2: There are 2^{2n-2} conditional rotation gates with 2n control qubits. According to the Corollary 7.12 in [38], the complexity of the n-qubit controlled rotation gate $R_y(2\varphi)$ is O (n) with an auxiliary qubit. Therefore, the complexity of the series of rotation gates is not greater than $O\left(n2^{2n-2}\right)$.

Operation 3: Since all quantum operations are implemented via unitary quantum gates, the quantum operations are invertible. So, the quantum circuit for the inverse non-block 1st-level transform can be implemented by reversing all of the gates of within non-block 1st-level decomposition. This results in the same complexity as the non-block transform, which is equal to 2n.

Adding the obtained results from the three operations leads to a total complexity of $O\left(n2^{2n-2}\right)$ for the non-block quantum watermark image embedding scheme.

By applying a similar analysis as above to the block quantum image embedding scheme shown in Fig. 15 and the non-block and block watermark image extraction schemes depicted in Fig. 17 and Fig. 18, respectively, we can conclude that the complexities of these methods are the same and in the order of $O\left(n2^{2n-2}\right)$.

VI. EXPERIMENTAL RESULTS AND ANALYSES

The presented watermarking schemes are simulated on classical computers using MATLAB due to the limited availability of quantum computers. MATLAB facilitates the representation and manipulation of large arrays of vectors and matrices, which makes it a suitable tool for simulating quantum states and quantum unitary operations. In particular, by treating the quantum images as large matrices, transformations can be simulated using linear algebraic operations equivalent to the quantum circuit elements. Moreover, complex vectors are used to simulate quantum effects, such as quantum entanglement or superposition, and quantum operators are simulated by unitary matrices.

The two quantum watermarking algorithms presented in this work are validated using a set of four classical 64 × 64 grayscale images as carrier images and four binary 32 × 32 watermark images. The carrier and watermark images are illustrated in Fig. 19, where (a), (b), (c) and (d) are the grayscale carrier images named Lena, Cameraman, Mandrill, and Pirate. Watermark images (e), (f), (g) and (h) are, respectively, the badge of Shanghai Maritime University (SHMTU), the badge of Research Center of Intelligent Information Processing and Quantum Intelligent Computing (RCIIP&QIC)) in addition to binary versions of reduced sizes of Lena and

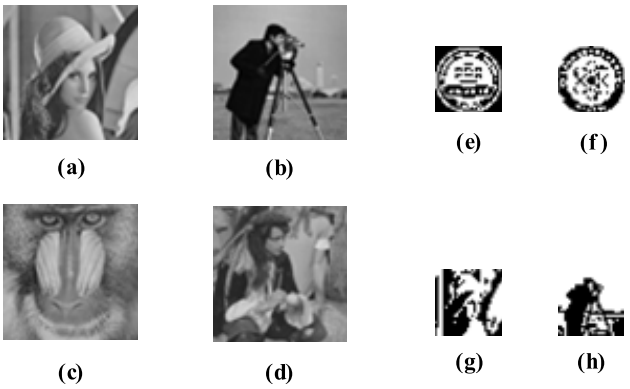

FIGURE 19. Original carrier images [(a) Lena, (b) Cameraman, (c) Mandrill, (d) Pirate] and watermark images [(e) SHMTU, (f) RCIIP&QIC, (g) Lena_W, (h) Cameraman_W].

Cameraman. We refer to the last two watermark images as Lena_W and Cameraman_W to distinguish them from their carrier image counterparts.

Theoretically, in a quantum noiseless environment, the proposed quantum image watermarking schemes can extract an error-free watermark image from quantum registers via quantum measurement operations. However, quantum (microscopic world) noise exists in reality and will affect the performance of the algorithms. Due to the lack of practical quantum computers to conduct the proposed quantum image watermarking schemes as well as the different noise nature in classical (macroscopic world) computers, the robustness analysis of the Stego images based on noise simulation under different hostile attack in quantum registers is not discussed in this paper.

A. IMPERCEPTIBILTY

Imperceptibility measures the similarity between the carrier images and the Stego images. To analyze the imperceptibility of the investigated non-block and block quantum watermarking schemes in detail, the Peak Signal to Noise Ratio (PSNR), similarity between two quantum images, and histogram analyses are considered.

1) PSNR

To quantitatively assess the visual quality of a Stego image compared to the original image, the PSNR for the two $2^n \times 2^n$ grayscale images are computed as follows:

$$PSNR = 20 \log 10 \frac{255}{\sqrt{1/2^{2n} \sum_{i=0}^{2^n-1} \sum_{j=0}^{2^n-1} [C(i,j) - S(i,j)]^2}} \tag{42}$$

where C represents the original carrier image and S denotes the corresponding Stego image.

The higher the similarity of the carrier images with their Stego versions, the greater the obtained PSNR. The watermarked images using the two different presented watermarking schemes (non-block and block methods) are illustrated in Figs. 20 and 21. A comparison of the non-block

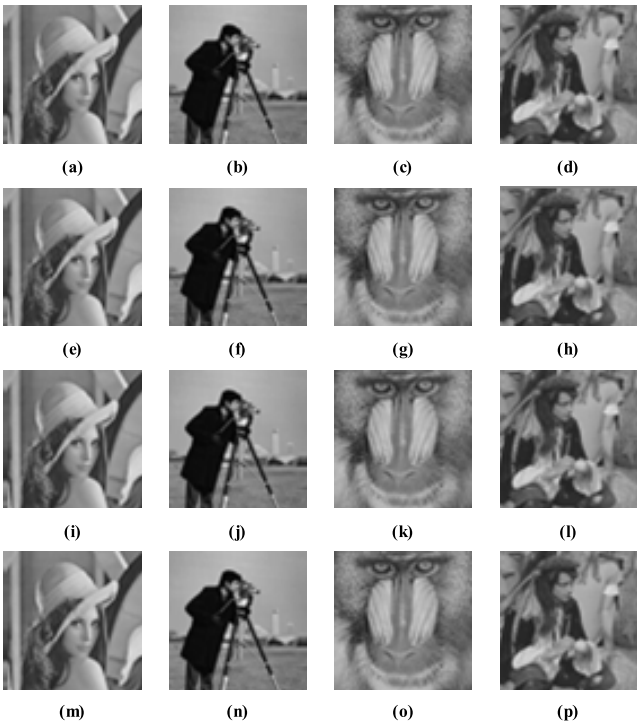

FIGURE 20. Watermarked images based on the non-block watermarking scheme. Stego images in the first to fourth rows are watermarked by the watermark images SHMTU, RCIIP&QIC, Lena_W, Cameraman_W, respectively.

TABLE 1. Similarity of stego images of our investigated schemes watermarked by SHMTU and RCIIP&QIC.

Methods	Carrier images \ Watermark images	SHMTU (dB)	RCIIP&QIC (dB)
non-block	Lena	64.9094	62.3792
	Cameraman	54.0882	53.9606
	Mandrill	67.5334	69.4832
	Pirate	65.2235	65.1696
block	Lena	64.9094	62.3792
	Cameraman	51.7600	51.8315
	Mandrill	67.5334	69.4832
	Pirate	65.2235	65.1696

and block watermarking schemes based on the PSNR is demonstrated in Table I and Table II. It can be observed that the two watermarking algorithms have very close visual quality as measured by the PSNR values for most of the tested images.

The PSNR values of both the non-block and block quantum image watermarking schemes are greater than 62dB except for the Cameraman image. The high PSNR values indicate that the Stego images have a high degree of similarity to the original images and that the watermarking process did not affect the visual effects of the carrier images. Additionally, it is not possible for the human eye to distinguish the difference between the carrier and stego images.

Based on the obtained PSNR values in Tables I and II, we can infer that the presented image watermarking schemes

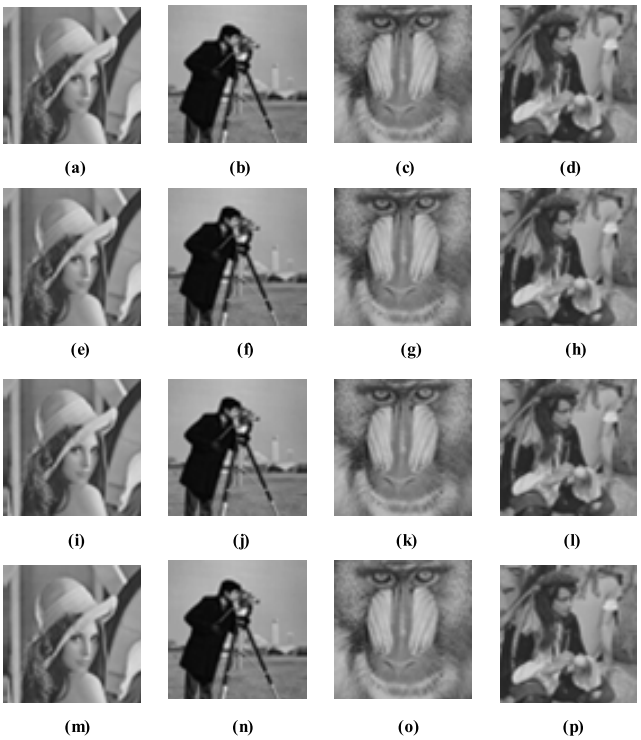

FIGURE 21. Watermarked images based on the block watermarking scheme. Stego images in the first to fourth rows are watermarked by the watermark images SHMTU, RCIIP&QIC, Lena_W, Cameraman_W, respectively.

TABLE 2. Similarity of stego images of our investigated schemes watermarked by Lena_W and Cameraman_W.

Methods	Carrier images \ Watermark images	Lena_W (dB)	Cameraman_W (dB)
non-block	Lena	71.0322	63.8012
	Cameraman	55.7664	67.5334
	Mandrill	68.2338	67.0944
	Pirate	65.5038	66.1253
block	Lena	71.0322	63.8012
	Cameraman	54.0799	67.5334
	Mandrill	68.2338	67.0944
	Pirate	65.5038	66.1253

have a higher similarity and in turn less effect on visual appearance of the images than the other watermarking schemes in the literature, such as in [20] (approximately 54 dB), [21] (58∼62 dB), [22] (58 dB), and [23] (55 dB).

2) SIMILARITY BETWEEN TWO QUANTUM IMAGES

Although the classical metric PSNR used demonstrates that the presented watermarking algorithm has excellent visual performance, it seems more convenient to utilize a quantum-based metric to assess the fidelity between two quantum images.

Here, we adopt the similarity evaluation metric proposed by Yan *et al.* [41], which can be used to compare the colors in two quantum images position-by-position. For two $2^n \times 2^n$

TABLE 3. Similarity analysis of carrier images and stego images by SHMTU and RCIIP&QIC using the quantum similarity metric (sim).

Methods	Watermark images / Carrier images	SHMTU	RCIIP&QIC
non-block	Lena	1.0000	1.0000
	Cameraman	0.9998	0.9999
	Mandrill	1.0000	1.0000
	Pirate	0.9999	0.9999
block	Lena	1.0000	1.0000
	Cameraman	0.9998	0.9999
	Mandrill	1.0000	1.0000
	Pirate	0.9999	0.9999

TABLE 4. Similarity analysis of carrier images and stego images by lena_w and cameraman_w using the quantum similarity metric (sim).

Methods	Watermark images / Carrier Images	Lena_W	Cameraman_W
non-block	Lena	1.0000	1.0000
	Cameraman	0.9998	1.0000
	Mandrill	1.0000	1.0000
	Pirate	1.0000	1.0000
block	Lena	1.0000	1.0000
	Cameraman	0.9998	1.0000
	Mandrill	1.0000	1.0000
	Pirate	1.0000	1.0000

FRQI images $|I_0\rangle$ and $|I_1\rangle$ expressed as follows:

$$|I_0\rangle = \frac{1}{2^n}\sum_{i=0}^{2^{2n}-1}\left(\cos\theta_0^i|0\rangle + \sin\theta_0^i|1\rangle\right)|i\rangle$$
$$|I_1\rangle = \frac{1}{2^n}\sum_{i=0}^{2^{2n}-1}\left(\cos\varphi_1^i|0\rangle + \sin\varphi_1^i|i\rangle\right)|i\rangle, \quad (43)$$

the similarity (sim) between two quantum images is defined by:

$$sim\left(|I_0\rangle, |I_1\rangle\right) = \frac{1}{2^{2n}}\sum_{i=0}^{2^{2n}}\cos\sigma_i,$$
$$\sigma_i = \left|\theta_0^i - \varphi_1^i\right|, \quad \sigma_i \in \left[0, \frac{\pi}{2}\right] \quad (44)$$

where θ_0^i and φ_1^i represent the pixel color information of $|I_0\rangle$ and $|I_1\rangle$ at position i, respectively, $\sigma_i = \left|\theta_0^i - \varphi_1^i\right|$ denotes the pixel difference at position i.

Tables III and IV show the similarities between the different pairs of carrier and corresponding Stego images. Note that some values are equal to 1.0000, which means the Stego images are almost identical to the carrier image. Moreover, all the values are greater than 0.9998, which indicates that the Stego images have excellent fidelity with the carrier images.

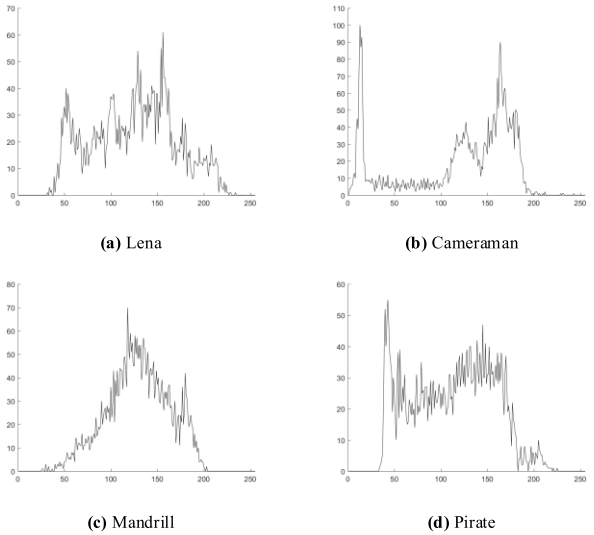

FIGURE 22. Histograms of original carrier images (a) Lena, (b) Cameraman, (c) Mandrill, and (d) Pirate.

3) HISTOGRAM GRAPH

The image's histogram can be considered another useful criterion for evaluating the fidelity of a Stego image compared with its original version. By comparing the histograms of the original images and watermarked images, the images' similarity can be determined from another perspective. The histogram graphs of four original carrier images are demonstrated in Fig. 22.

Figures 23 and 24 are the histogram graphs of the Stego images that are watermarked by the watermark image SHMTU using non-block and block watermarking algorithms. Obviously, compared to the histograms' graphs of the original carrier images, the Stego images' histograms are highly consistent with their original counterparts. Thus, the existence of watermark image information is efficiently hidden into the Stego images.

B. ROBUSTNESS

Bit Error Rate (BER) is defined as the inverse of PSNR as follows:

$$BER = \frac{1}{PSNR} \quad (45)$$

The BER determines the percentage of original image bits that change during the watermarking procedure. For example, if the PSNR is 40 dB, the BER would be 0.025. This means that 2.5% of the bits changed during the watermarking process. The results of the BER values of the Stego images calculated in the performed simulations are given in Table V. Since all of the BER values are less than 0.019, i.e., more than 98.18% of the bits remained unchanged. This indicates that the introduced algorithms embed the watermark image information while slightly affecting the original image.

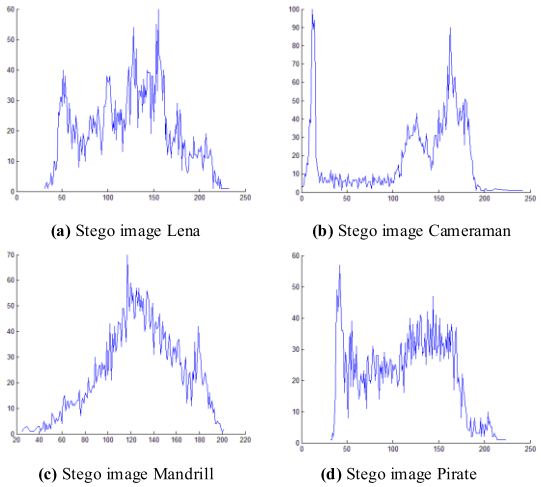

(a) Stego image Lena (b) Stego image Cameraman

(c) Stego image Mandrill (d) Stego image Pirate

FIGURE 23. Histograms of stego images using non-block watermarking schemes. (a), (b), (c) and (d) are the histogram images of the watermarked images Lena, Cameraman, Mandrill, and Pirate. The watermark image is SHMTU.

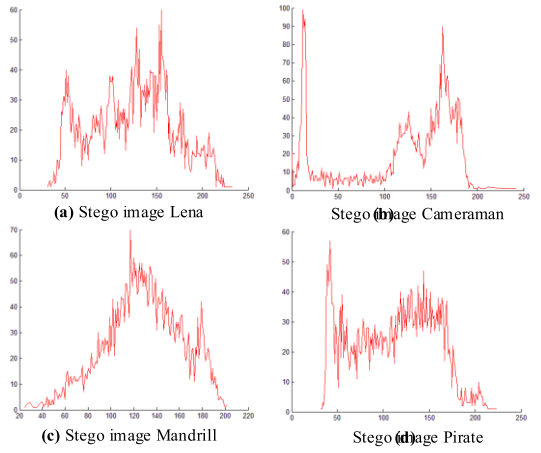

(a) Stego image Lena Stego image Cameraman (b)

(c) Stego image Mandrill Stego image Pirate (d)

FIGURE 24. Histograms of Stego images using block watermarking schemes. (a), (b), (c) and (d) are the histogram images that respectively belong to the watermarked images Lena, Cameraman, Mandrill, and Pirate. The watermark image is SHMTU.

TABLE 5. Bit error rate (BER) values of the investigated watermarking schemes.

Methods	Watermark images / Carrier images	BER SHMTU	BER RCIIP&QIC
non-block	Lena	0.015	0.016
	Cameraman	0.018	0.019
	Mandrill	0.015	0.014
	Pirate	0.015	0.015
block	Lena	0.015	0.016
	Cameraman	0.019	0.016
	Mandrill	0.015	0.014
	Pirate	0.015	0.015

C. CAPACITY

The capacity of a watermarking scheme is defined as the ratio of the number of message bits to the number of carrier image pixels as follows:

$$Capacity = \frac{the\ number\ of\ message\ bits}{the\ number\ of\ carrier\ image's\ pixel} \quad (46)$$

Since the introduced watermarking schemes embed a $2^{n-1} \times 2^{n-1}$ binary image into a $2^n \times 2^n$ grayscale carrier image, the proposed watermarking algorithms' capacity is calculated as:

$$C = \frac{2^{n-1} \times 2^{n-1}}{2^n \times 2^n} = \frac{1}{4} bits/pixel \quad (47)$$

In other word, one message bit is inserted on average in four pixels for the presented watermarking scheme, which is greater than [21] ($1/16$ $bits/pixel$) and equal to [22].

VII. CONCLUSION

A quantum image watermarking scheme in the frequency domain based on the decomposition of QHWT for FRQI images is proposed in this paper. The algorithms embed a $2^{n-1} \times 2^{n-1}$ binary watermark image into a $2^n \times 2^n$ grayscale carrier image. Based on non-block and block 1^{st}-level decomposition for an FRQI image, two quantum watermark image embedding schemes as well as their integrated quantum circuit implementations are provided. Both methods insert the watermarking information by slightly changing the diagonal wavelet coefficients in the frequency domain of the carrier images. In the non-block watermarking method, the diagonal wavelet coefficients in the entire original image are modified while the image is divided into blocks and the diagonal wavelet coefficients in each block are changed separately in the block watermarking method.

The introduced watermarking methods are simulated and tested via a set of carrier and watermark images. The experimental results demonstrate the high degree of similarity between the Stego images and carrier images as measured by PSNR, quantum similarity metric, and histograms. Moreover, the obtained low bit error rate for all tested images indicates that only a small fraction of the image bits are changed. This confirms the high similarity between the Stego image and carrier image, and shows the modifications introduced by the watermarking information to the carrier image are subtle and will be undetected by the human eye. As evident from the results, the quantum realization of the presented watermarking algorithms is highly efficient.

REFERENCES

[1] J. Stajic, "The future of quantum information processing," *Science*, vol. 339, no. 6124, p. 1163, 2013.
[2] R. P. Feynman, "Simulating physics with computers," *Int. J. Theor. Phys.*, vol. 21, nos. 6–7, pp. 467–488, 1982.
[3] M. A. Nielsen and I. L. Chuang, *Quantum Computation and Quantum Information*. Cambridge, U.K.: Cambridge Univ. Press, 2000.
[4] P. W. Shor, "Algorithms for quantum computation: Discrete logarithms and factoring," in *Proc. 35th Annu. IEEE Symp. Found. Comput. Sci.*, Nov. 1994, pp. 124–134.
[5] D. Deutsch, "Quantum theory, the church-turing principle and the universal quantum computer," *Proc. R. Soc. Lond. A, Math. Phys. Sci.*, vol. 400, no. 1818, pp. 97–117, Jul. 8, 1985.

[6] G. Brassard, P. Hoyer, L. K. Grover, D. Deutsch, R. Jozsa, and P. W. Shor, "A fast quantum mechanical algorithm for database search," in *Proc. 5th Israeli Symp. Theory Comput. Syst.*, 1992, pp. 212–219.

[7] A. M. Iliyasu, "Towards realising secure and efficient image and video processing applications on quantum computers," *Entropy*, vol. 15, no. 8, pp. 2874–2974, 2013.

[8] F. Yan, A. M. Iliyasu, and P. Q. Le, "Quantum image processing: A review of advances in its security technologies," *Int. J. Quantum Inf.*, vol. 15, no. 3, p. 1730001, 2017.

[9] F. Yan, A. M. Iliyasu, and S. E. Venegas-Andraca, "A survey of quantum image representations," *Quantum Inf. Process.*, vol. 15, no. 1, pp. 1–35, 2016.

[10] S. E. Venegas-Andraca and S. Bose, "Storing, processing, and retrieving an image using quantum mechanics," *Proc. SPIE*, vol. 5105, pp. 134–147, Aug. 2003.

[11] S. E. Venegas-Andraca and J. L. Ball, "Processing images in entangled quantum systems," *Quantum Inf. Process.*, vol. 9, no. 1, pp. 1–11, 2010.

[12] P. Q. Le, F. Dong, and K. Hirota, "A flexible representation of quantum images for polynomial preparation, image compression, and processing operations," *Quantum Inf. Process.*, vol. 10, no. 1, pp. 63–84, 2011.

[13] Y. Zhang, K. Lu, Y. Gao, and M. Wang, "NEQR: A novel enhanced quantum representation of digital images," *Quantum Inf. Process.*, vol. 12, no. 8, pp. 2833–2860, Aug. 013.

[14] Y. Zhang, K. Lu, Y. Gao, and K. Xu, "A novel quantum representation for log-polar images," *Quantum Inf. Process.*, vol. 12, no. 9, pp. 3103–3126, 2013.

[15] H.-S. Li, Q. Zhu, R.-G. Zhou, L. Song, and X.-J. Yang, "Multi-dimensional color image storage and retrieval for a normal arbitrary quantum superposition state," *Quantum Inf. Process.*, vol. 13, no. 4, pp. 991–1011, 2014.

[16] S. Yuan, X. Mao, Y. Xue, L. Chen, Q. Xiong, and A. Compare, "SQR: A simple quantum representation of infrared images," *Quantum Inf. Process.*, vol. 13, no. 6, pp. 1353–1379, 2014.

[17] H.-S. Li, X. Chen, H. Xia, Y. Liang, and Z. Zhou, "A quantum image representation based on bitplanes," *IEEE Access*, vol. 6, pp. 62396–62404, 2018.

[18] H.-S. Li, P. Fan, H.-Y. Xia, H. Peng, and S. Song, "Quantum implementation circuits of quantum signal representation and type conversion," *IEEE Trans. Circuits Syst. I, Reg. Papers*, vol. 66, no. 1, pp. 341–354, Jan. 2019.

[19] I. Cox, *Digital Watermarking and Steganography*. San Mateo, CA, USA: Morgan Kaufmann, 2007.

[20] R.-G. Zhou, W. Hu, and P. Fan, "Quantum watermarking scheme through Arnold scrambling and LSB steganography," *Quantum Inf. Process.*, vol. 16, no. 9, pp. 1–21, Sep. 2017.

[21] G. Luo, R. Zhou, W. Hu, J. Luo, X. Liu, and H. Ian, "Enhanced least significant qubit watermarking scheme for quantum images," *Quantum Inf. Process.*, vol. 17, no. 11, p. 299, Nov. 2018.

[22] W. Hu, R.-G. Zhou, J. Luo, and B. Liu, "LSBs-based quantum color images watermarking algorithm in edge region," *Quantum Inf. Process.*, vol. 18, no. 1, p. 16, Jan. 2019.

[23] S. Heidari and E. Farzadnia, "A novel quantum LSB-based steganography method using the Gray code for colored quantum images," *Quantum Inf. Process.*, vol. 16, no. 10, pp. 1–28, Oct. 2017.

[24] W.-W. Zhang, F. Gao, B. Liu, Q.-Y. Wen, and H. Chen, "A watermark strategy for quantum images based on quantum Fourier transform," *Quantum Inf. Process.*, vol. 12, no. 2, pp. 793–803, 2013.

[25] X.-H. Song, S. Wang, S. Liu, A. A. A. El-Latif, and X.-M. Niu, "A dynamic watermarking scheme for quantum images using quantum wavelet transform," *Quantum Inf. Process.*, vol. 12, no. 12, pp. 3689–3706, 2013.

[26] X. Song, S. Wang, A. A. A. El-Latif, and X. Niu, "Dynamic watermarking scheme for quantum images based on Hadamard transform," *Multimedia Syst.*, vol. 20, no. 4, pp. 379–388, 2014.

[27] I. Daubechies, *Ten Lectures on Wavelets* (Number 61 in CBMS-NSF Series in Applied Mathematics), Philadelphia, PA, USA: SIAM, 1992.

[28] M. Rabbani, "JPEG2000: Image compression fundamentals, standards and practice," *J. Electron. Imag.*, vol. 11, no. 2, p. 286, 2002. doi: 10.1117/1.1469618.

[29] X.-G. Xia, C. G. Boncelet, and G. R. Arce, "Wavelet transform based watermark for digital images," *Opt. Express*, vol. 3, no. 12, pp. 497–511, 1998.

[30] P. Meerwald and A. Uhl, "Survey of wavelet-domain watermarking algorithms," *Proc. SPIE*, vol. 4314, pp. 505–516, Aug. 2001.

[31] L. Ruiz-Perez and J. C. Garcia-Escartin, "Quantum arithmetic with the quantum Fourier transform," *Quant. Inf. Process.*, vol. 16, no. 6, p. 152, Jun. 2017.

[32] A. Fijany and C. P. Williams, "Quantum wavelet transforms: Fast algorithms and complete circuits," in *Quantum Computing and Quantum Communications—QCQC* (Lecture Notes in Computer Science), vol. 1509, C. P. Williams, Ed. Berlin, Germany: Springer, 1999.

[33] Y.-G. Yang, X. Jia, S.-J. Sun, and Q.-X. Pan, "Quantum cryptographic algorithm for color images using quantum Fourier transform and double random-phase encoding," *Inf. Sci.*, vol. 277, pp. 445–457, Sep. 2014.

[34] H.-S. Li, C. Li, X. Chen, and H.-Y. Xia, "Quantum image encryption algorithm based on NASS," *Int. J. Theor. Phys.*, vol. 57, no. 12, pp. 3745–3760, 2018.

[35] Y.-G. Yang, X. Jia, P. Xu, and J. Tian, "Analysis and improvement of the watermark strategy for quantum images based on quantum Fourier transform," *Quantum Inf. Process.*, vol. 12, no. 8, pp. 2765–2769, Aug. 2013.

[36] Y.-G. Yang, P. Xu, J. Tian, and H. Zhang, "Analysis and improvement of the dynamic watermarking scheme for quantum images using quantum wavelet transform," *Quantum Inf. Process.*, vol. 13, no. 9, pp. 1931–1936, 2014.

[37] Y.-G. Yang, Y. Wang, and Q.-Q. Zhao, "Letter to the editor regarding 'Dynamic watermarking scheme for quantum images based on Hadamard transform' by Song *et al.*," *Multimedia Syst.*, vol. 22, no. 2, pp. 271–272, 2016.

[38] A. Barenco, C. H. Bennett, R. Cleve, D. P. DiVincenzo, N. Margolus, P. Shor, J. Smolin, and H. Weinfurter, "Elementary gates for quantum computation," *Phys. Rev. A, Gen. Phys.*, vol. 52, pp. 3457–3488, Nov. 1995.

[39] J.-S. Guf and W.-S. Jiang, "The Haar wavelets operational matrix of integration," *Int. J. Syst. Sci.*, vol. 27, no. 7, pp. 623–628, 1996.

[40] P. Porwik and A. Lisowska, "The Haar-wavelet transform in digital image processing: Its status and achievements," *Mach. Graph. Learn.* , vol. 13, nos. 1–2, pp. 79–98, 2004.

[41] F. Yan, P. Q. Le, A. M. Iliyasu, B. Sun, J. A. Garcia, F. Dong, and K. Hirota, "Assessing the similarity of quantum images based on probability measurements," in *Proc. IEEE Congr. Evol. Comput. (CEC)*, Jun. 2012, pp. 1–6. doi: 10.1109/CEC.2012.6256418.

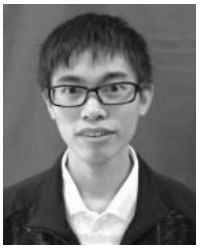

WEN-WEN HU received the B.S. degree in mathematics and computer from Wuyi University, Fujian, China, in 2015, and the M.S. degree in computer application technology from East China Jiaotong University, Nanchang, Jiangxi, China, in 2018. He is currently pursuing the Ph.D. degree in information system with Shanghai Maritime University, Shanghai, China. His research interests include the quantum information processing, quantum communication, digital image processing, and quantum image processing.

RI-GUI ZHOU (M'12) was born in March 1973. He received the B.S. degree from Shandong University, China, in 1997, the M.S. degree from the Department of Computer Science and Technology, Nanchang Hangkong University, China, in 2003, and the Ph.D. degree from the Department of Computer Science and Technology, Nanjing University of Aeronautics and Astronauts, China, in 2007.

From 2008 to 2010, he was a Postdoctoral Fellow with Tsinghua University, China. From 2010 to 2011, he held a Postdoctoral position at Carleton University, Ottawa, Canada. From 2014 to 2015, he was a Visiting Scholar with North Carolina State University, Raleigh, NC, USA. He is currently a Professor with the College of Information Engineering, Shanghai Maritime University, China. His main research interests include quantum image processing, quantum reversible logic, and quantum genetic algorithm.

Prof. Zhou is also a Senior Member of the China Computer Federation (CCF). He was a recipient of the New Century Excellent Talents Program from the Ministry of Education of China, in 2013.

AHMED EL-RAFEI received the B.Sc. degree (Hons.) in electronics and communication engineering and the M.Sc. degree in engineering mathematics from Ain Shams University, and the Dr.Eng. degree (Hons.) in computer science from the University of Erlangen-Nuremberg, Germany, in 2012. From 2012 to 2018, he was an Assistant Professor with the Engineering Physics and Mathematics Department, Faculty of Engineering, Ain Shams University, where he was a Teaching and Research Assistant and is currently an Associate Professor. He joined the University of Erlangen-Nuremberg, as a Guest Professor, in 2015. In 2018, he was a Visiting Scholar with Shanghai Maritime University, China. He has authored/coauthored many international peer-reviewed conference and journal articles in addition to supervising master's and Ph.D. theses. His research interests include applied mathematics in engineering, signal and medical image processing, machine learning, quantum information processing, and artificial intelligence. He is also a member of the Egyptian Society of Language Engineering. He has been a member of the Erlangen School of Advanced Optical Technologies SAOT and the Association for Research in Vision and Ophthalmology (ARVO). He is also a Reviewer of many international journals and research grants in addition to being part of the scientific committee of scientific conferences.

SHE-XIANG JIANG is currently pursuing the Ph.D. degree in information system with Shanghai Maritime University, Shanghai, China. His research interests include quantum image processing, quantum communication, quantum teleportation, and remote state preparation.